Revision 2 Word Count: 9521

Multiple fluid sources in skarn systems: Oxygen isotopic evidence from the Haobugao Zn-Fe-Sn deposit in the southern Great Xing'an Range, NE China

Lijie Liu[a,b], Taofa Zhou[a*], Bin Fu[c], Trevor R. Ireland[c], Dayu Zhang[a], Guangxian Liu[a], Feng Yuan[a], Xiangping Zha[d], Noel C. White[a,e],

a Ore Deposit and Exploration Center (ODEC), School of Resources and Environmental Engineering, Hefei University of Technology, Hefei 230009, China

b State Key Laboratory of Geological Processes and Mineral Resources, Collaborative Innovation Center for Exploration of Strategic Mineral Resources, School of Earth Resources, China University of Geosciences, Wuhan 430074, China.

c Research School of Earth Sciences, The Australian National University, Canberra ACT 2601, Australia

d School of Earth and Space Sciences, University of Science and Technology of China, Hefei, 230026, China

e Centre for Ore Deposit and Earth Sciences, University of Tasmania, Hobart, Tas 7000, Australia

* Corresponding author. E-mail address: tfzhou@hfut.edu.cn (Taofa Zhou)

Abstract

Diverse fluid sources and complex fluid flow paths in skarn systems appear to be well documented. Nevertheless, in situ microanalysis of oxygen isotopes by secondary ion microprobe (SIMS) in skarn minerals can provide further high spatial resolution information on this complexity and the formation of skarns and associated ore deposits. In this study, we investigated the Haobugao skarn Zn-Fe-Sn deposit (0.36 M tonnes Zn) in the southern Great Xing'an Range, NE China, and the associated Early Cretaceous Wulanba biotite granite. Based on drill hole logging, four early skarn

phases are recognized: proximal red-brown garnet-hedenbergite exoskarn, central green garnet exoskarn, light brown garnet-diopside exoskarn, and distal pyroxene skarn. Oxygen isotope analyses of garnet, pyroxene and other minerals from skarn, oxide, and quartz-sulfide stages were carried out by SIMS to determine the origin and evolution of the skarn-forming hydrothermal system. Garnet from exoskarn has a much wider range in $\delta^{18}O_{VSMOW}$, between –8.1 and +6.0‰, than other stages and minerals. The estimated $\delta^{18}O$ values of fluids in equilibrium with the Haobugao skarn vary widely from –5.1‰ to +8.9‰, suggesting that the skarn formed via episodic flux of magmatic fluid and meteoric water. Low $\delta^{18}O$ values of cassiterite and quartz from quartz-sulfide stage rocks are +1.2 to +3.6‰, and +5.7 to +5.9‰, respectively, indicating significant contributions of meteoric water during deposition of Pb-Zn sulphides. Therefore, meteoric fluids were periodically present throughout most of the stages of skarn formation at Haobugao.

Keywords: oxygen isotopes; skarn; meteoric water; magmatic fluid; fluid source; Haobugao

1 Introduction

Skarn ore deposits are important global sources of base (W, Cu, Fe, Mo, Sn, Pb, and Zn) and precious (Au and Ag) metals; they form in association with shallow magmatic systems that were emplaced in or near carbonate rocks (Meinert, 1992; 1997; Chang et al., 2019). Many studies have been carried out to determine the source, properties (e.g. temperature, salinity, pH, pressure) and evolution of the ore-forming fluids (Meinert et al., 1997, 2003, 2005; Crowe et al., 2001; Singoyi and Zaw, 2001; Baker et al., 2004; Rossetti et al., 2008; Samson et al., 2008; Vallance et al., 2009; D'Errico et al., 2012; Peng et al., 2015; Shu et al., 2011; 2017; Zhong et al.,

2018; Demir and Dişliet, 2020). The origin and evolution of skarn-related ore-forming fluids remain incompletely understood with two general competing models: (1) Pre-ore skarn formed by magmatic fluids, and ore precipitation resulting from mixing of magmatic fluids with low-$\delta^{18}O_{VSMOW}$ meteoric water (Shelton, 1983; Layne and Spooner, 1991; Singoyi and Zaw, 2001; Palinkaš et al., 2013; Peng et al., 2015; Shu et al., 2017; Zhong et al., 2018; Demir and Dişliet, 2020); (2) Both early fluids in the prograde skarn stage and later ore-forming fluids in the retrograde stage correspond to different pulses of magmatic fluids released at different stages of magma differentiation, as based on the magmatic oxygen isotope signatures of hydrothermal alteration minerals and fluid inclusion analyses (Meinert et al., 1997, 2003; Baker and Lang, 2003; Baker et al., 2004; Samson et al., 2008; Vallance et al., 2009; Shu et al., 2011). Megaw (1998) and Meinert et al. (2005) have pointed out that both increased involvement of external fluids and interaction with wall rocks are to be expected with increasing distance from magmatic fluid sources.

Oxygen isotopes have long been recognized as a powerful tracer of magmatic and hydrothermal processes largely based on bulk oxygen isotope analyses of single minerals in these systems (e.g., Christensen et al., 1989; Clechenko and Valley, 2003; Demir and Dişliet, 2020; Gevedon et al., 2021). Garnets can be zoned in cations (Fe, Mg, Mn, and Ca) and trace elements (Tracy et al., 1976; Hickmott et al., 1987; Jamtveit, 1991; Jamtveit et al., 1993, 1995). Thus, Crowe et al. (2001) found oxygen isotope zoning in hydrothermal garnets and became the first to publish integrated isotope and elemental data at microanalytical scale, which has greatly improved the understanding of the formation of hydrothermal garnets. Moreover, there are typically spatio-temporal chemical zoning in crystals in skarn hydrothermal systems (Kwak and Tan, 1981; Meinert, 1997), and recent in-situ LA-ICP-MS trace element

analytical work demonstrated that the main and trace elements in some other minerals (e.g., pyroxene, apatite) are also heterogeneous, which further indicates that the formation of individual minerals probably results from different fluid sources and formation conditions (Zhao et al., 2020; Liu et al., 2021a), however, they are lacking of oxygen isotope constraints. D'Errico et al. (2012) suggested that high-$\delta^{18}O$ magmatic and/or metamorphic water were added into the Empire Mountain skarn system dominated by meteoric fluid infiltration. Ryan-Davis et al. (2019) reported that meteoric fluid may be present during at least some stages of garnet formation throughout Mineral King in two of the localities. Therefore, in-situ oxygen isotopic microanalysis of garnets and other minerals can provide a valuable tracer for detailing changes in hydrothermal fluids (Lackey et al., 2012; D'Errico et al., 2012; Russel et al., 2013; Higashino et al., 2019; Ryan-Davis et al., 2019; Rottier et al., 2021; Li et al., 2022).

The Haobugao deposit is a typical skarn Zn-Fe-Sn deposit in the southern Great Xing'an Range, NE China. Studies of the ore-forming fluids of this deposit by oxygen isotopic work commonly focused on quartz of oxide and quartz-sulfide stages and suggest mixing of magmatic fluid and meteoric water (Li et al., 2015; Liu et al., 2017; Wang et al., 2018). Shu et al (2021) analyzed in-situ fluid inclusion compositions by LA-ICP-MS and bulk oxygen isotope compositions of quartz from different mineralization stages, and found that the prograde fluids were magmatic and mixing with meteoric water caused later dilution and Zn-Pb deposition. Given that garnets in the Haobugao deposit developed different generations (Fan et al., 2019; Liu et al., 2021a) and less attention has been paid to the fluid from which cassiterite precipitated, the fluid source and fluid evolution of the Haobugao Zn-Fe-Sn deposit still need to be further investigated. In this study, we present petrological,

compositional and oxygen isotope data for zoned garnets together with pyroxene, vesuvianite, tremolite, cassiterite, magnetite, quartz, and calcite from different stages of the Haobugao Zn-Fe-Sn deposit in the southern Great Xing'an Range, NE China, with the aim of constraining the fluid sources and providing a systematic record of the evolution of the skarn-forming hydrothermal system.

2 Geological setting

The southern Great Xing'an Range (SGXR) is located in the eastern part of the Central Asian Orogenic Belt. It is bordered as a wedge-shape zone by the Xilamulun Fault in the south, the Erlianhaote-Hegenshan Fault in the northwest, and the Nenjiang Fault in the east (Fig.1a). The rocks exposed in this area are mainly Permian sedimentary rocks and Mesozoic volcanic rocks and granites (Fig.1b). Faults with NE-, NNE-, E- and NW-trending are well developed. Numerous porphyry Cu-Mo, skarn Fe-Sn-Cu-Pb-Zn and epithermal Pb-Zn-Ag deposits developed in this region, which makes it the largest tin and copper polymetallic belt in North China (Wang et al., 2005). These deposits are temporally and spatially associated with Jurassic and Cretaceous intrusions (Mao et al., 2005), and nearly 90% of deposits are hosted within Permian rocks (Sheng and Fu, 1999; Liu et al., 2004).

The Haobugao deposit is one of the largest skarn Fe-Zn-Sn polymetallic deposits in the southern Great Xing'an Range, NE China (Fig. 1a). There are 7.72 million tonnes of iron ore, with an average grade of 32.41 wt.%. The estimated resource of zinc is 0.36 million tonnes (4.00 wt.%). In addition, it contains 15,766 tonnes Cu (0.90 wt.%) and 6,760 tonnes Pb (1.73 wt.%). The skarn is hosted within the Permian Dashizhai Formation, which consists of marine pyroclastic rocks, slate, argillaceous siltstone, and marble (Figs. 1c and 2). The ores formed during the Early Cretaceous when the

Wulanba biotite granite was emplaced in an extensional tectonic setting (U-Pb Zircon age of 142.9 ± 1.6 Ma; Liu et al., 2018, 2021b). NE-trending faults are the ore-controlling structures (Sheng and Fu, 1999). The ore-forming fluids in the skarn stage are characterized by medium-high temperature (330 to 420°C) and intermediate to high salinity brines (5 to 13 wt.% and 35 to 39 wt.% NaCl equiv.); the ore-forming fluids of the quartz-sulfide stage are characterized by low-medium temperature (110 to 355°C) and low salinity aqueous fluids (1 to 13 wt.% NaCl equiv.) (Li et al., 2015). In the field, the skarn shows color and composition variations, with endoskarn featured by green chlorite alteration (Fig. 3a), early proximal zone red garnet-pyroxene skarn (Fig. 3b), central zone green garnet exoskarn (Fig. 3c) and light brown garnet-diopside skarn (Fig. 3d), and late distal zone dark green pyroxene skarn (Figs. 3e and 3f). Such variations are related to the distance from the biotite granite. The abundance of garnet in skarn gradually increases from 20% to 50% by volume, and the pyroxene content gradually decreases from 50% to 10% with increasing depth (Fig. 2; Bai, 1996; Xiao et al., 2004), similar to what is observed in many other typical skarn deposits (Meinert et al., 2005). Five skarn mineralization stages are recognized in the Haobugao deposit (Fig. 4), and they are early skarn stage, late skarn stage, oxide stage, early and late quartz-sulfide stage. Early skarns are dominated by anhydrous skarn minerals, including garnet and pyroxene, which partly replaced wollastonite that formed earlier. The late skarn stage consists of vesuvianite, amphibole, tremolite and minor cassiterite. The oxide stage is characterized by a mineral assemblage of abundant magnetite and minor cassiterite, quartz and chlorite. Magnetite, amphibole, chlorite and other hydrous minerals replaced some of the early skarn minerals. The early quartz-sulfide stage is comprised of arsenopyrite, pyrite, molybdenite, chalcopyrite, sphalerite, quartz, chlorite and minor fluorite. The late

quartz-sulfide stage is characterized by abundant sphalerite, galena, calcite, quartz and fluorite (Figs. 4 and 5).

3 Sample descriptions and occurrence

In order to give a systematic description of the Haobugao skarn, 20 representative samples of skarn, oxide, and early and late quartz-sulfide stages were collected from drill hole cores (ZK2509, ZK1708, ZK2511, ZK2510) and the open pit. Sample ZK2511-869 was collected from proximal exoskarn and consists of garnet and pyroxene (Figs. 2 and 3e). Samples ZK2511-454, ZK2511-423, ZK2511-438, ZK2511-369 and ZK2510-468 collected from the central exoskarn consist of garnet, pyroxene, magnetite, and minor sulfides (Figs. 2, 3c, 3d, 5g and 5i). Samples ZK2510-29 and ZK2511-79 are distal exoskarn with pyroxene, quartz and sulfides (Figs. 2, 3a, 3b, 5e and 5f). Cassiterite collected from the open pit is closely associated with garnet and amphibole (Fig. 5l).

4 Analytical methods

4.1 EMP (Electron Microprobe)

Chemical compositions of minerals were analyzed and back scatter images (BSE) image taken using a JAX-8230 electron microprobe in the Department of Geology, School of Resource and Environmental Engineering, Hefei University of Technology, China (Shi, 2016). The operating conditions were 15 kV accelerating voltage and 20 nA beam current. Natural minerals were used as standards, and the ZAF program was utilized for matrix corrections. The analytical uncertainties of elements are 2% (Si), 5% (Fe and Mg) and 25% (Ti, Al, Cr, Mn, Ca, Na and K) by mass, respectively. Mineral formulae of clinopyroxene were calculated based on 6 oxygens.

176 **4.2 Laser Fluorination**

177 The in-house standard measurements for hedenbergite, tremolite and vesuvianite were
178 performed using laser fluorination analysis in School of Earth and Space Science,
179 University of Science and Technology of China, Hefei (Gong and Zheng, 2003).
180 Samples were crushed, washed and sieved. Hedenbergite was handpicked clean under
181 a binocular microscope. Aliquots of hedenbergite and garnet standard (04BXL07)
182 were pretreated with BrF_5 at a lower pressure (< 0.3×10^5 Pa) overnight prior to
183 analysis. Using an IR laser (λ=10.6 μm) and a Finnigan/MAT 251 gas-source mass
184 spectrometer, hedenbergite grains were fluorinated and sample O_2 was converted to
185 CO_2 via a hot graphite rod prior to being introduced to the mass spectrometer for
186 analysis. The same method and data treatment were also applied to analyses of
187 tremolite and vesuvianite. Data were reported to the VSMOW scale based on multiple
188 analyses of garnet standard (04BXL07, +3.70‰; Gong et al., 2007), with an
189 analytical uncertainty of ±0.10‰ (2S.D.).
190

191 **4.3 SIMS (Secondary Ion Mass Spectroscopy)**

192 In situ oxygen isotope measurements of garnet, diopside, hedenbergite, tremolite,
193 vesuvianite, cassiterite and quartz were performed using the SHRIMP SI multi-
194 collector ion microprobe in Research School of Earth Sciences, Australian National
195 University, Canberra, with a Cs^+ primary beam accelerated at 15 keV with an
196 intensity of ~5 nA. The resulting beam spot was elliptical with an average size of ~25
197 μm, as measured on SEM images after the SHRIMP SI analysis. Details of the
198 instrumental conditions can be found in Martin et al. (2014) and Ávila et al. (2020).
199 Oxygen isotope ratios ($^{18}O/^{16}O$) are reported in $\delta^{18}O$ notation relative to VSMOW.
200 The UWG-2 garnet was used as primary standard ($\delta^{18}O$ +5.8‰, Valley et al., 1995)

and reproduced over the analytical sessions with a standard deviation of better than ±0.60‰ (2S.D.). The data for garnet were further corrected for matrix effects of grossular, spessartine and andradite in garnet, similar to that of Martin et al. (2014) because the calibration may vary from session to session. The compositional bias corrections range from +3.2 to +6.8‰. The primary standard for diopside is UWC3 (or 95AK24; $\delta^{18}O$ = +10.18‰; Edwards and Valley, 1998; Kozdon et al., 2009) and reproduced a standard deviation from ±0.46‰ to ±0.63‰ (2S.D.). Both 97SL65 diopside and NRM-AG1 clinopyroxene are used as monitoring standards (Fu et al., 2003; Deegan et al., 2016). The data for pyroxenes were further corrected for matrix effects of ferrosilite/hedenbergite and wollastonite in pyroxene (B. Fu, unpublished data), with compositional bias corrections range from –0.7 to +1.3‰. Detailed information on Yankee cassiterite (+2.0‰), quartz standards UWQ1 (+12.33‰) and NBS-28 (+9.59‰) can be found in Carr et al. (2017), Kelly et al. (2017) and Spicuzza et al. (1998), respectively. The reproducibility of Yankee cassiterite, UWQ1 and NBS-28 quartz standards is ±0.72‰, ±0.70‰ and ±0.58‰ (2S.D.), respectively. The measurement precision of calcite is ±0.36‰ (2S.D.) based on replicate measurements of the reference material NBS-19 (+28.64‰; International Atomic Energy Agency, 1995).

5 Results

5.1 Mineral compositions

The garnets analyzed were dominantly grossular-andradite solid solutions, with a total of almandine + pyrope + spessartine typically < 2 mol.%. Proximal red-brown garnets contain significant amounts of Al ($Adr_{49-41}Grs_{47-54}$). Central zone green garnets are enriched in Fe with $Adr_{63-97}Grs_{2-34}$. These garnets commonly have Fe-rich cores and

Al-rich oscillatory zoned rims. Central zone light brown garnets are typically grossular-rich with $Adr_{49-51}Grs_{48-50}$ (Fig. 6a), the compositions of which are homogeneous within both crystals and samples. Proximal dark green pyroxene is hedenbergite with $Di_{9-11}Hd_{81-90}$, which replaced red-brown garnet (Figs. 3b and 6b). Pyroxenes from the central exoskarn are diopside with $Di_{64-88}Hd_{11-33}$. Pyroxenes in distal exoskarn are mainly hedenbergite ($Di_{19-41}Hd_{56-77}$), with minor diopside ($Di_{88}Hd_{11}$). Early diopside has been replaced by hedenbergite (Fig. 6b). The EMP results of garnet are reported in Liu et al. (2021a) and the representative chemical compositions of pyroxene are listed in Table S1.

5.2 Oxygen isotope compositions

SIMS results of garnets are listed in Table 1. While proximal red garnet has homogeneous oxygen isotope compositions, with $\delta^{18}O$ varying from +4.1 to +4.7‰ and with an average of +4.5‰, central zone green garnet has a wide range in $\delta^{18}O$, between –8.1 and +6.0‰. In detail, $\delta^{18}O$ in single garnet grains from the central exoskarn is highly variable, from –8.1 to +2.0‰, with an average of –1.6‰ (Fig. 7). The central zone light yellow-brown garnet from the exoskarn has relatively constant $\delta^{18}O$, +5.0 to +5.6‰, and averaging at +5.4‰ (Fig. 7). The largest $\delta^{18}O$ intragrain variation was observed in a zoned garnet crystal (Sample ZK2510-468) which shows an abrupt increase in $\delta^{18}O$ (by 10.1‰) from core to rim (Fig. 8c). Andradite from central green exoskarn displays different $\delta^{18}O$ trends (Fig. 8): 'V' shape for Sample ZK2511-454, i.e., a decrease from core to mantle, then an increase to rim (Fig. 8d); fluctuating $\delta^{18}O$ pattern for Sample ZK2511-438 (Fig. 8b); and flat or homogeneous core and a decrease from core to rim for Sample ZK2510-369 (Fig. 8a).

Oxygen isotope values of +0.3‰, +5.7‰ and +3.9‰ were obtained by laser

fluorination for hedenbergite (ZK2511-869), tremolite (ZK2511-162) and vesuvianite (ZK1708-618), respectively. The results are shown in Table S2. Further SIMS analysis indicates that $\delta^{18}O$ in proximal hedenbergite (ZK2511-869) varies from –0.8 to +1.8‰, assuming that the average is +0.3‰ as above, whereas hedenbergite in the distal exoskarn (ZK2510-79) has a wider range in $\delta^{18}O$, from –2.6 to +0.9‰ (avg. –0.4‰; Fig. 7; Table 2). Likewise, $\delta^{18}O$ values of vesuvianite and tremolite from the late skarn stage range between +3.4 and +4.4‰ (avg. +3.9‰), and from +5.3 to +6.1‰ (avg. +5.7‰), respectively (Table 3).

Diopside has $\delta^{18}O$ values of +2.7 to +4.8‰ (avg. +3.9‰), for the central green exoskarn; uniform $\delta^{18}O$ values of +5.0±0.1‰ (2s), for the central light brown exoskarn; and uniform $\delta^{18}O$ values of +6.3±0.1‰ (2s), for the distal exoskarn. A pyroxene crystal from the distal exoskarn sample ZK2510-29 consists of diopside in the core and hedenbergite in the rim (Fig. 9a). These two different components have distinct $\delta^{18}O$ values, with diopside displaying higher $\delta^{18}O$ values (Fig. 9b).

Cassiterite from the oxide stage cutting primary garnetite has $\delta^{18}O$ values from +1.2 to +3.6‰, averaging at +2.4‰ (Table 4).

There are two groups of quartz: (1) high $\delta^{18}O$, from +7.0 to +12.5‰, with an average of +8.4‰, for early quartz-sulfide stage; from +8.2 to +8.6‰, for quartz phenocryst from biotite granite; (2) low $\delta^{18}O$, from –3.9 to +3.9‰, avg. –0.5‰, for quartz from the late quartz-sulfide stage (Table 5).

6 Discussion

6.1 Oxygen isotopic homogeneity and equilibrium

Oxygen isotope ratios of minerals in the Haobugao skarn deposit at both intragrain and intergrain scales are evaluated here. In general, most of the mineral grains

analyzed are relatively homogeneous in $\delta^{18}O$, except some garnet grains from central green exoskarn and pyroxene crystals from distal exoskarn, as shown in tables and Fig. 7. Contrasting $\delta^{18}O$ features of the same kind of mineral at different stages can be recognized. Previous studies correlated positive relationship between Fe (andradite) with $\delta^{18}O$ values (Crowe et al., 2001; Clechenko and Valley, 2003; Page et al., 2010). This is apparently not the case at Haobugao, because $\delta^{18}O$ remains constant while the andradite component in garnet varies (Figs. 8c and 8e) or variation in $\delta^{18}O$ is not coupled with change of andradite content (Fig. 8d), which are similar to the Empire Mountain, Sierra Nevada (D'Errico et al., 2012). Additionally, unlike vesuvianite, tremolite and cassiterite in many samples that do not show significant $\delta^{18}O$ intergrain variations, $\delta^{18}O$ of quartz in Sample ZK2509-327 ranges from +7.5 to +12.5‰ (Fig. 5i). This might be caused by the reopening of the quartz vein by different hydrothermal fluids in the system. At the deposit scale, garnet, pyroxene, cassiterite and quartz have large variations in $\delta^{18}O$, from –8.1 to +5.6‰, –0.6 to +6.3‰, –1.2 to +3.6‰ and –3.9 to +12.5‰, respectively. The lowest garnet $\delta^{18}O$ value (–8.1‰) is comparable with that (–8.8‰) of garnet measured by SIMS at White Chief (Ryan-Davis et al. 2019) and (–8.9‰) by laser fluorination by Gevedon et al. (2021).

Normally, the isotopic composition of the coexisting minerals follows the equilibrium order ($\delta^{18}O$: quartz > calcite > diopside > garnet) (Zheng et al., 1993a, b). Any reverse order or misalignment may indicate that the coexisting minerals are in isotopic disequilibrium, formed either from different stages, or at different temperatures, or underwent post-crystallization isotopic exchange such as diffusion (Zheng et al., 1993a, b). Accordingly, the grossular-hedenbergite pair (ZK2511-869) is out of isotopic equilibrium because grossular has higher $\delta^{18}O$ values than hedenbergite. This is consistent with the observation that grossular was altered to hedenbergite (Fig. 3b).

$\delta^{18}O$ value of diopside (5.0‰) is slightly lower than grossular (5.0–5.6‰) in sample ZK2511-423 (Fig. 8f). It's difficult to judge whether they were in isotopic equilibrium or not due to limited SIMS analytical precision. Diopside from sample ZK2510-468 has higher $\delta^{18}O$ value of 4.1‰ than that of andradite rim (–0.2‰) (Fig. 8c), and a calculated equilibrium temperature of 0 ℃ can be obtained using the method of Zheng et al. (1993a). The extremely low temperature suggests they were not in isotopic equilibrium and diopside probably precipitate later. The estimated temperature for garnet and pyroxene is obviously inconsistent with the fluid inclusion data for the Haobugao deposit. Li et al. (2015) and Wang et al. (2018) suggested that the ore-forming fluids of garnet form the early skarn stage are characterized by intermediate-high temperature of 330–420°C and 320–420°C, respectively. Wang (2017) and Shu et al. (2021) reported higher homogenization temperatures of diopside from the early skarn stage, with 390–550°C and 420–575°C, respectively. Given small $\delta^{18}O$ variation (even within 0.6‰, 2S.D.) can result in large range of calculated temperatures, as well as the fact that the proposed temperature variation (150℃) would not change the calculated $\delta^{18}O_{fluid}$ greatly, temperatures used for calculating $\delta^{18}O_{fluid}$ of the early skarn stage are assumed to be 500℃ based on the relatively more realistic fluid inclusion work. Additionally, Wang (2017) recorded that homogenization temperatures of calcite from late skarn stage are 310–480°C; Wang et al. (2018) reported that homogenization temperatures of quartz-magnetite stage are 285–440°C. Fluids of quartz-sulfide stage are featured by low temperature (110–360°C), with early quart-sulfide stage has slightly higher temperatures (Li et al., 2015; Wang, 2017; Wang et al., 2018; Shu et al., 2021). This is consistent with the calculated temperature (215℃) of quartz-calcite (ZK1708-566) from the late quartz-sulfide stage, based on the calibration of Sharp and Kirschner (1994). Therefore,

temperatures used for calculating $\delta^{18}O_{fluid}$ of late skarn stage, oxide stage, and early and late quartz-sulfide stages are estimated to be 450℃, 400℃, 300℃ and 200℃ respectively. The $\delta^{18}O$ values of the fluid ($\delta^{18}O_{fluid}$) in equilibrium with the minerals were calculated using the oxygen isotope fractionation factors for garnet and pyroxene (Zheng et al., 1993a), vesuvianite and tremolite (Zheng et al., 1993b), cassiterite (Zhang et al., 1994) and quartz (Clayton et al., 1972), respectively. The calculated isotopic compositions of the fluid in equilibrium are shown in Tables 1, 2 and 3.

6.2 Multiple fluid sources

Fluids assumed in oxygen isotope equilibrium with the Haobugao skarns have a large variation in $\delta^{18}O$, from –5.1 to +8.9‰, which is beyond the range of $\delta^{18}O_{fluid}$ (−0.9‰ to +9.1‰) interpreted form ore-forming fluids in the pre- and main-ore stages of the major late Mesozoic ore deposits in the SGXR by Ouyang et al. (2015), especially for the lowest $\delta^{18}O_{fluid}$. Such a large range suggests that multiple fluid sources could be involved in the formation of Haobugao skarn: high-$\delta^{18}O$ magmatic/metamorphic fluids and low-$\delta^{18}O$ meteoric water. $\delta^{18}O_{fluid}$ of the biotite granite from the Haobugao deposit (ZK2509-894, ZK2509-1065 and ZK2509-1296) has an average of 8.2‰ at a solidus temperature of 800 ℃, which is consistent with the $\delta^{18}O$ of magmatic fluids investigated by Clayton et al. (1972) and Crowe et al. (2001). Consequently, the low $\delta^{18}O$ values cannot be caused by fluids in equilibrium exchange with granite. The $\delta^{18}O$ values of calcite in marble from the ore district is +9.8 to +13.9‰, with an average of +12.1‰ (Liu et al., 2017), and devolatilization in a rock-dominated system without infiltrating fluids could lower $\delta^{18}O$ values of silicate-bearing carbonate by no more than +2 to +4‰ (Valley, 1986; Bowman, 1998). Therefore, the low $\delta^{18}O$ values

could not be produced by fluid interactions with the marble, but with significant involvement of meteoric water or a lower-$\delta^{18}O$ meteoric fluid source due to the presence of glacial meltwater, as temperature variations of 150°C would only change the calculated $\delta^{18}O_{fluid}$ by less than ±1.5‰ (Crowe et al., 2001). In addition, the $\delta^{13}C_{PDB}$ values for calcite from ore range from –9.9‰ to –5.5‰ whereas the calcite from marble has distinctly high values between +2.9 and +4.8‰ (Liu et al., 2017), which also suggests fluids at Haobugao are not a rock buffered system.

Yang et al. (2013) reported extremely low $\delta^{18}O$ values (–18.12‰ to –13.19‰) of hydrothermal zircon form the Baerzhe granite in the SGXR, and attributed the low $\delta^{18}O$ values to the addition of meteoric water, transported by glaciers during the early Aptian in NE China. Globally, the ice cap or sheet mostly occurred in high palaeo-latitude area during the Valanginian, Barremian, Aptian and early Albian (Price, 1999; Amiot et al., 2011) and in low palaeo-latitude area during the late Barremian-mid-Albian, i.e., all during the early Cretaceous (Steuber et al., 2005; Yang et al., 2013). Haobugao skarn formed at 142.9 ± 1.6 Ma, a time which is considered to have had a hot climate (Littler et al., 2011). Therefore, the low $\delta^{18}O$ values of Haobugao skarn system should be caused by the input of meteoric water, not the continental ice sheet. Zhao et al. (1994) suggested the $\delta^{18}O_{fluid}$ of Mesozoic groundwater in the Great Xing'an Range is around –16‰. Liu et al. (2008) further indicated that $\delta^{18}O$ value of precipitation in this area is around –10‰ which is likely to be the same in the early Cretaceous. Thus, surface-derived meteoric water must be a significant component of the fluid budget of the skarn-forming hydrothermal system, accounting for the low $\delta^{18}O$ values in Haobugao skarn, and the meteoric water incorporated into the skarn by direct mixing with magmatic fluid.

The highest $\delta^{18}O_{fluid}$ value can up to +8.9‰, which is slightly higher than the oxygen

375 isotopic composition of fluids (+8.2‰) evolved from the biotite granite. This highest
376 number is regarded within the range of magmatic water, considering the small
377 deviation of 0.6‰ and analytical errors, and further indicates that magmatic water can
378 account for the high $\delta^{18}O_{fluid}$ in Haobugao skarn system.

379 **Early skarn stage**: Proximal red-brown grossular has slightly lower and
380 homogeneous $\delta^{18}O_{fluid}$ values (+7.1 to +7.7‰, avg. +7.5‰) than biotite exsolved
381 water, suggesting that the fluids are magmatic water dominated. By comparison,
382 proximal hedenbergite has an average $\delta^{18}O_{fluid}$ value of +2.6‰ which are much lower
383 than those of the adjacent grossular, indicating it mainly formed from meteoric water.
384 These distinctly different $\delta^{18}O_{fluid}$ values indicate that the proximal exoskarn formed
385 from two different fluids. This is consistent with the fact that the earlier formed
386 proximal grossular was replaced to the later hedenbergite (Figs. 3b and 9).

387 In contrast, both andradite and diopside from central green exoskarn show wide
388 $\delta^{18}O_{fluid}$ variations, from –5.1 to +8.9‰ and +4.6 to +6.7‰, respectively; and central
389 light brown grossular and diopside show similar and constant $\delta^{18}O_{fluid}$ values:
390 +8.2±0.3‰ and +6.9±0.1‰, respectively (Fig. 10). The wide range of $\delta^{18}O_{fluid}$ of
391 andradite suggests mixing of diverse and fluctuating fluids, resulting in major changes
392 in the fluid composition. The later grossular and diopside are magmatic in origin as
393 reflected by their $\delta^{18}O$ values.

394 Diopside (+8.2±0.1‰) and hedenbergite (+2.8 to +5.3‰) from the distal exoskarn
395 have distinct $\delta^{18}O_{fluid}$ values (Fig. 10). Diopside shows a magmatic origin, with a
396 higher proportion of magmatic fluid compared to some of the intermediate-depth
397 skarn, suggesting fracture-controlled fluid flow. It appears that the distal diopside is
398 very likely originated form the same magmatic pulse as the later central grossular. The
399 later hedenbergite formed when more meteoric water was incorporated in the fluids.

Late skarn stage: $\delta^{18}O_{fluid}$ calculated from vesuvianite and tremolite varies from +6.8 to +8.5‰ (avg. +7.7‰; Table 2). Thus, the hydrous skarn minerals of late skarn stage also formed from the magmatic fluid.

Oxide stage: Fluid $\delta^{18}O$ estimated from cassiterite ranges from +4.9 to +7.4‰, and is markedly different from that of magnetite (+2.5 to +2.7‰; Liu et al., 2017). The lower $\delta^{18}O_{fluid}$ of this stage than the late skarn stage suggests that cassiterite and magnetite precipitated from mixed fluids of magmatic and meteoric water. The $\delta^{18}O_{fluid}$ values further indicate these two minerals are not in isotopic equilibrium, although some tiny cassiterite inclusion was found in magnetite. Magnetite formed with more involvement of meteoric water.

Quartz-sulfide stage: $\delta^{18}O_{fluid}$ values of quartz coexisting with molybdenite, arsenopyrite, chalcopyrite and fluorite from the early quartz-sulfide stage range from –5.5‰ to +5.6‰ (avg. –0.1‰), implying mixing of meteoric and magmatic water; quartz intergrown with chalcopyrite, sphalerite, galena, calcite and fluorite from the late quartz-sulfide stage has $\delta^{18}O_{fluid}$ of –15.6‰ to –7.8‰ (averaging –11.5‰). This suggests that the quartz-sulfide stage was meteoric water dominated, and the decrease of $\delta^{18}O_{fluid}$ from early to late quartz-sulfide stages indicates an overwhelming amount of meteoric water poured into the system at the latest stage (Fig. 10).

6.3 Formation of the skarn hydrothermal system and its implications

From samples collected throughout the deposit, a record of temporal and spatial variations in fluid-rock interaction can be obtained. The biotite granite in the Haobugao skarn deposit was emplaced at a depth of 2 km, as revealed by fluid inclusion studies, promoting fracturing of its wall-rocks. Initially, the proximal grossular with $\delta^{18}O$ value of 4.5‰ precipitated from magmatic dominated fluid (Fig. 11a). Absence of $\delta^{18}O$ zonation in garnet suggests that the proximal garnet grew under

425 a relatively restricted range of temperature and fluid composition, which might be
426 caused by diffusive metasomatism. With the transition from lithostatic to hydrostatic
427 pressure, more fractures formed allowing greater ingress of meteoric water. At this
428 stage, the central green exoskarn garnet skarn formed. Due to pore fluids from
429 adjacent units came out under hydrostatic pressure and with sluggish fluid-rock
430 reaction rate at ambient crustal temperatures prior to large amount of skarn formation,
431 garnet with low $\delta^{18}O_{fluid}$ values (–5.1% to –3.2%) precipitated. Mixing at different
432 times of varying proportions of magmatic water, meteoric water and less likely
433 metamorphic fluid led to andradite with different $\delta^{18}O$ compositions observed (Figs. 8
434 and 11a). Although low-$\delta^{18}O$ garnets can have formed exclusively by brecciation and
435 without the presence of surface fluids as suggested by Ramos et al. (2018), they
436 instead sourced form ^{18}O-depleted pore fluids of adjacent units. Given the large
437 amount of low-$\delta^{18}O$ green andradite in the central exoskarn, the low $\delta^{18}O$ values of
438 green andradite were more likely to be caused by surface meteoric water infiltration.
439 Then light brown grossular and diopside skarn which partly overprinted andradite
440 skarn precipitated from the magmatic fluid. Permeability was maintained by the
441 growth of garnet and other skarn minerals, due to their higher density than the
442 minerals they replaced. Distal diopside formed from distal fluids dominated by
443 magmatic water (Fig. 11a). Finally, the proximal and distal hedenbergite with low
444 $\delta^{18}O$ values overgrew the previously-formed minerals (Fig. 11b), which indicates that
445 meteoric water can infiltrate down to the top of the intrusion during the late stage of
446 skarn formation, which might be caused by fracture-controlled fluid flow (D'Errico et
447 al., 2012). Meteoric water continued to invade the hydrothermal system, lowering the
448 temperature and diluting the metal-transporting complexes (Einaudi and Burt, 1982;
449 Hemley et al., 1992; Fournier, 1999; Crowe et al., 2001; Meinert et al., 2005;

Schwinn et al., 2006). Fluid mixing caused deposition of the Haobugao metalliferous ores, with minor influence of reaction with carbonate together (Figs.7 and 9). Lowered element concentrations and Pb/(Na + K) and Zn/(Na + K) ratios in the quartz-sulfide-stage fluid inclusions also revealed mixing of magmatic water with meteoric fluid caused dilution and Zn-Pb deposition (Shu et al., 2021). Cassiterite precipitation occurred at low degrees of dilution by meteoric water, followed by deposition of magnetite, sphalerite and galena (Figs. 11c and 11d).

Overall, distinct temporal transitions from magmatic- to meteoric-dominated fluids suggest periodic increased flux of magmatic fluid occurred in the Haobugao skarn system. This is strongly indicated by the common occurrence of prograde mineral of different generation, or prograde and retrograde assemblages in the same hand specimen at the same location, which is inconsistent with a single fluid model (Fig. 9). To explain the coexistence of early and late mineral assemblages, the single fluid model needs pre-ore fluids to be stagnant until groundwater mixes with it at late stage (Shu et al., 2017). The extremely low $\delta^{18}O_{fluid}$ of central exoskarn grossular core (ZK2510-468) implies that considerable meteoric water was involved in the skarn system even at its earliest stage, which could be a supplement for the consensus where magmatic water dominated in early stage of skarn formation in the SGXR and worldwide (Meinert et al., 2005; Öztürk and Helvaci, 2008; Palinkaš et al., 2013; Peng et al., 2015; Ouyang et al., 2015).

The typical model involving increased involvement of external fluids and interaction with wall rocks with increasing distance from magmatic fluid sources during skarn formation is not what happened at Haobugao. The probable reason is that the wall rocks, as illustrated in the 25th cross section, consist mainly of siltstone and slate, which have low permeability, and minor marble, which during skarn formation allows

475 the magmatic fluids to diffuse upwards. This is consistent with the observation that
476 proximal garnet skarn was not well developed at Haobugao. Fluid-rock interactions
477 were constrained along lithologic contacts and were controlled by fractures. Repeated
478 pulses of magmatic fluid extended long distances and overprinted the early skarn
479 features, as illustrated in the fluid flow model (Fig. 11).
480

481 **7 Implications**

482 A systematic study of petrology, composition and in-situ oxygen isotope of the
483 Haobugao Zn-Fe-Sn deposit provides new insights into fluid sources and fluid
484 evolution in skarn system, as follows.
485 (1) Garnets at Haobugao precipitated from aqueous fluids that were predominantly of
486 magmatic and meteoric origin and mixtures thereof. Mixing of these components
487 occurred at the start of the skarn stage. Meteoric fluids during garnet formation
488 further supports what recent studies have shown.
489 (2) There are multiple stages of hydrothermal fluid at Haobugao; and episodic flux of
490 magmatic fluid was recorded in the skarn minerals. The amount of meteoric water did
491 not increase with the decreasing depth and the central exoskarn displays complex
492 fluid mixing.
493 (3) The hydrothermal system involved fluctuating contributions of magmatic and
494 meteoric fluids, however, the latest stage associated with deposition of Pb-Zn
495 mineralization was predominately associated with an influx of meteoric water.
496

497 **Acknowledgements**

498 This research was jointly supported by National Natural Science Foundation of China
499 (Grant No. 91962218), China Geological Survey (Grant No. 12120115033801) and

the Fundamental Research Funds for the Central Universities of China (Grant No. PA2019GDZC0093). The authors acknowledge the support of Inner Mongolia Chifeng Institute of Geology and Mineral Exploration Development for their valuable help during the fieldwork. The first author acknowledges the financial support of the China Scholarship Council during his stay in Australia. Thanks are due to Dr. P. Holden (ANU) for assistance with SHRIMP analysis and Prof. Y.-F. Zheng (USTC) and Prof. S.-Y. Jiang (CUG) for discussion. The authors also appreciate Editor Dr. J.S. Lackey and anonymous reviewers for their valuable suggestions which have improved the quality of this paper substantially.

References cited list

Amiot. R., Wang. X., Zhou, Z.H., Wang, X.L., Buffetaut, E., Lécuyer, C., Ding, Z.L., Fluteau, F., Hibino, T., Kusuhashi, N., Mo, J.Y., Suteethorn, V., Wang, Y.Q., Xu, X., and Zhang, F.S. (2011) Oxygen isotopes of East Asian dinosaurs reveal exceptionally cold Early Cretaceous climates. Proceedings of the National Academy of Sciences of the United States of America, 108(13), 5179–5183.

Ávila, J.N., Ireland, T.R., Holden, P., Lanc, P., Latimore, A., Schram, N., Foster, J., Williams, I.S., Loiselle, L., and Fu, B. (2020) High-Precision, High-Accuracy Oxygen Isotope Measurements of Zircon Reference Materials with the SHRIMP-SI. Geostandards and Geoanalytical Research, 44(1), 85–102.

Bai, D.M. (1996) Application of geologic, geophysical, geochemical prospecting method in the Haobugao Pb–Zn–Sn–Cu polymetallic deposit. Geological Exploration for Non-ferrous Metals, 5(6), 361–367 (in Chinese with English abstract)

Baker, T., Achterberg, E. V., Ryan, C. G., and Lang, J. R. (2004) Composition and

525 evolution of ore fluids in a magmatic-hydrothermal skarn deposit. Geology,
526 32(2), 117.
527 Baker, T., and Lang, J.R. (2003) Reconciling fluid inclusions, fluid processes and
528 fluid source in skarns: An example from the Bismark skarn deposit, Mexico.
529 Mineralium Deposita, 38, 474–495.
530 Bowman, J.R. (1998) Stable isotope systematics of skarns. Mineralogical Association
531 of Canada Short Course Handbook, 26, 99–146.
532 Carr, P. A., Norman, M. D., and Bennett, V. C. (2017) Assessment of crystallographic
533 orientation effects on secondary ion mass spectrometry (SIMS) analysis of
534 cassiterite. Chemical Geology, 467, 122–133.
535 Chang, Z.S., Shu, Q.H., and Meinert, L.D. (2019) Skarn deposits of China. Economic
536 Geology, 22, 189–234.
537 Christensen, J.N., Rosenfeld, J.L., and Depaolo, D.J. (1989) Rates of tectono-
538 metamorphic processes from rubidium and strontium isotopes in garnet. Science,
539 244(4911), 1465–1469.
540 Clayton, R.N., O'Neil, J.R., and Mayeda, T.K. (1972) Oxygen isotope exchange
541 between quartz and water. Journal of Geophysical Research, 77, 3057–3067.
542 Clechenko, C.C., and Valley, J.W. (2003) Oscillatory zoning in garnet from the
543 Willsboro Wollastonite Skarn, Adirondack Mts, New York: a record of shallow
544 hydrothermal processes preserved in a granulite facies terrane. Journal of
545 metamorphic. Geology, 21, 771–784.
546 Crowe, D.E., Riciputi, L.R., Bezenek, S., and Ignatiev, A. (2001) Oxygen isotope and
547 trace element zoning in hydrothermal garnets: windows into large-scale fluid-
548 flow behavior. Geology, 29(6), 479.
549 Demir, Y., and Dişli, A. (2020) Fluid inclusion and stable isotope constraints (C, O,

H) on the Dağbaşı Fe–Cu–Zn skarn mineralization (Trabzon, NE Turkey). Ore Geology Reviews, 116, https://doi.org/10.1016/j.oregeorev.2019.103235.

Deegan, F.M., Whitehouse, M.J., Troll, V.R., Budd, D.A., Harris, C., Geiger, H., and Hålenius, U. (2016) Pyroxene standards for SIMS oxygen isotope analysis and their application to Merapi volcano, Sunda arc, Indonesia. Chemical Geology, 447, 1–10.

D'Errico, M.E., Lackey, J.S., Surpless, B.E., Loewy, S.L., Wooden, J.L., and Barnes, J.D. (2012) A detailed record of shallow hydrothermal fluid flow in the Sierra Nevada magmatic arc from low-$\delta^{18}O$ skarn garnets. Geology, 40(8), 763–766.

Edwards, K.J., and Valley, J.W. (1998) Oxygen isotope diffusion and zoning in diopside: The importance of water fugacity during cooling. Geochimica Et Cosmochimica Acta, 62(13), 2265–2277.

Einaudi, M.T., and Burt, D.M. (1982) Introduction-terminology, classification, and composition of skarn deposits. Economic Geology, 77, 745–754.

Fan, X.J., Wang, X.D., Lü, X.B., Wei, W., and Chen, W. (2019) Garnet composition as an indicator of skarn formation: LA-ICP-MS and EPMA studies on oscillatory zoned garnets from the Haobugao skarn deposit, Inner Mongolia. Journal of China Geology, 54, 1976–1992.

Fournier, R.O. (1999) Hydrothermal processes related to movement of fluid from plastic into brittle rock in the magmatic epithermal environment. Economic Geology, 94, 1193–1211.

Fu, B., Touret, J.L.R., Zheng, Y.F. (2003) Remnants of premetamorphic fluid and oxygen isotopic signatures in eclogites and garnet clinopyroxenite from the Dabie-Sulu terranes, eastern China. Journal of metamorphic Geology, 21(6), 561–578.

575 Gevedon, M., Lackey, J.S., Barens, J.D. (2021) Skarn fluid sources as indicators of
576 timing of Cordilleran arc emergence and paleogeography in the southwestern
577 United States. Geology, 49(11), 1317–1321.
578 Gong, B., and Zheng, Y.F. (2003) A CO2-laser technique for oxygen isotope analysis
579 of silicates. Earth Science Frontiers, 10(2), 279–286 (in Chinese with English
580 abstract).
581 Gong, B., Zheng, Y.F., and Chen, R.X. (2007) TC/EA-MS online determination of
582 hydrogen isotope composition and water concentration in eclogitic
583 garnet. Physics and Chemistry Minerals, 34(10), 687–698.
584 Hemley, J.J., Cygan, G.L., Fein, J.B., Robinson, G.R., and D'Angelo, W.M. (1992)
585 Hydrothermal ore-forming processes in the light of studies in rock-buffered
586 systems; I, Iron-copper-zinc-lead sulfide solubility relations. Economic Geology,
587 87, 1–22.
588 Hickmott, D.D., Shimizu, N., Spear, F.S., and Selverstone, J. (1987) Trace-element
589 zoning in a metamorphic garnet. Geology, 15(6), 573–576.
590 Higashino, F., Rubatto, D., Kawakami, T., Bouvier, A.S., and Baumgartner, L.P.
591 (2019). Oxygen isotope speedometry in granulite facies garnet recording
592 fluid/melt–rock interaction (Sør Rondane Mountains, East Antarctica). Journal of
593 Metamorphic Geology, 37(7), 1037–1048.
594 International Atomic Energy Agency (1995) Reference and intercomparison materials
595 for stable isotopes of light elements.
596 Jamtveit, B. (1991) Oscillatory zonation patterns in hydrothermal grossular-andradite
597 garnet; nonlinear dynamics in regions of immiscibility. American Mineralogist,
598 76(7-8), 1319–1327.
599 Jamtveit, B., Wogelius, R.A., and Fraser, D.G. (1993) Zonation patterns of skarn

garnets: records of hydrothermal system evolution. Geology, 21, 113–116.

Jamtveit, B., Ragnarsdottir, K.V., and Wood, B.J. (1995) On the origin of zoned grossular-andradite garnets in hydrothermal systems. European Journal of Mineralogy, 7(6), 1399–1410.

Kelly, J. L., Fu, B., Kita, N. T., and Valley, J. W. (2007) Optically continuous silcrete quartz cements of the St. Peter Sandstone: high precision oxygen isotope analysis by ion microprobe. Geochimica Et Cosmochimica Acta, 71(15), 3812–3832.

Kozdon, R., Ushikubo, T., Kita, N.T., Spicuzza, M., and Valley, J.W. (2009) Intratest oxygen isotope variability in the planktonic foraminifer N. pachyderma: Real vs. apparent vital effects by ion microprobe. Chemical Geology, 258(3–4), 327–337.

Kwak, T., and Tan, T.H. (1981) The geochemistry of zoning in skarn minerals at the king island (Dolphin) mine. Economic Geology, 76(2), 468–497.

Lackey, J.S., Romero, G.A., Bouvier, A.S., and Valley, J.W. (2012) Dynamic growth of garnet in granitic magmas. Geology, 40(2), 171–174.

Layne, G.D., Longstaffe, F.J., and Spooner, E.T.C. (1991) The JC tin skarn deposit, southern Yukon Territory: II, A carbon, oxygen, hydrogen, and sulfur stable isotope study. Economic Geology, 86(1):48-65.

Li, J.F., Wang, K.Y., Lu, J.S., Zhang, X.B., Quan, H.Y., and Wang, C.Y. (2015) Ore - forming fluid geochemical characteristics and genesis of Pb-Zn deposit in Hongling, Inner Mongolia. Earth Science-Journal of China University of Geoscience, 40(6), 995-1005 (in Chinese with English abstract).

Li, Y., Zhang, R.Q., He, S., Chiaradia, M., and Li, X.H. (2022) Pulsed exsolution of magmatic ore-forming fluids in tin-tungsten systems: a SIMS cassiterite oxygen isotope record. Mineralium Deposita, 57(3), 343–352.

Liu, J.M., Zhang, R., and Zhang, Q.Z. (2004) The regional metallogeny of Da

Hinggan Ling, China. Earth Science Frontiers, 11, 269–277 (in Chinese with English abstract).

Littler, K., Robinson, S., Bown, P. Nederbragt, A.J., and Pancost, R.D. (2011) High sea-surface temperatures during the Early Cretaceous Epoch. Nature Geoscience, 4, 169–172.

Liu, L.J., Zhou, T.F., Zhang, D.Y., Yuan, F., Liu, G.X., Zhao, Z.C., Sun, J.D., and White, N. (2018) S isotopic geochemistry, zircon and cassiterite U–Pb geochronology of the Haobugao Sn polymetallic deposit, Southern Great Xing'an Range, NE China. Ore Geology Reviews, 93, 168–180.

Liu, L.J., Zhou, T.F., Zhang, D.Y., Yuan, F., Liu, G.X., Zhao, Z.C., Sun, J.D., and White, N. (2021a) Major and trace elements analyses of garnet from the Haobugao Zn-Fe-Sn polymetallic deposit, northeast China: Implications for skarn formation and hydrothermal fluid evolution. Ore Geology Reviews, 138 https://doi.org/10.1016/j.oregeorev.2021.104337.

Liu, L.J., Zhou, T.F., Fu, B., Zhang, D.Y., Yuan, F., Liu, G.X., White, N., and Hollings, P. (2021b). Petrogenesis of early cretaceous granitic rocks from the Haobugao area, southern Great Xing'an Range, northeast China: Geochronology, geochemistry and Sr-Nd-Hf-O isotope constraints. Lithos, 406-407 https://doi.org/10.1016/j.lithos.2021.106501

Liu, Y., Jiang, S.H., Bagas, L., Han, N., Chen, C.L., and Kang, H. (2017) Isotopic (C-O-S) geochemistry and Re–Os geochronology of the Haobugao Zn–Fe deposit in Inner Mongolia, NE China. Ore Geology Reviews, 130–147.

Liu, Z.F., Tian, L.D., Chai, X.R., and Yao, T.D. (2008) A model-based determination of spatial variation of precipitation $\delta^{18}O$ over china. Chemical Geology, 249(1), 203–212.

650 Mao, J.W., Xie, G.Q., Zhang, Z.H., Li, X.F., Wang, Y.T., Zhang, C.Q., and Li, Y.F.
651 (2005) Mesozoic large-scale metallogenic pulses in North China and
652 corresponding geodynamic settings. Acta Petrologica Sinica, 21(1), 169–188 (in
653 Chinese with English abstract).
654 Martin, L.A.J., Rubatto, D., Crépisson, Céline, Hermann, J., Putlitz, B., and Vitale-
655 Brovarone, A. (2014) Garnet oxygen analysis by Shrimp-SI: matrix corrections
656 and application to high-pressure metasomatic rocks from Alpine Corsica.
657 Chemical Geology, 374–375, 25–36.
658 Megaw, P., Ruiz, J., and Titley, S. (1988) High temperature, carbonate-hosted Ag-Pb-
659 Zn (Cu) deposits of northern Mexico. Economic Geology, 83, 1856–1885.
660 Meinert, L.D. (1992) Skarns and skarn deposits. Geoscience Canada, 19(4), 145–162.
661 Meinert, L.D., Dipple, G.M., and Nicolescu, S. (2005) World skarn deposits.
662 Economic Geology, 299–336.
663 Meinert, L.D., Hedenquist, J.W., Satoh, H., and Matsuhisa, Y. (2003) Formation of
664 anhydrous and hydrous skarn in Cu-Au ore deposits by magmatic fluids.
665 Economic Geology, 98, 147–156.
666 Meinert, L.D., Hefton, K.K, Mayes, D., and Tasiran, I. (1997) Geology, zonation, and
667 fluid evolution of the Big Gossan Cu-Au skarn deposit, Ertzberg district, Irian
668 Jaya. Economic Geology, 92, 509–534.
669 Ouyang, H.G., Mao, J.W., Zhou, Z.H., and Su, H.M. (2015) Late Mesozoic
670 metallogeny and intracontinental magmatism, southern Great Xing'an Range,
671 northeastern China. Gondwana Research, 27, 1153–1172.
672 Öztürk, Y.Y., and Helvaci, C. (2008) Skarn alteration and Au–Cu mineralization
673 associated with tertiary granitoids in northwestern turkey: evidence from the
674 Evciler deposit, Kazdag massif, Turkey. Economic Geology, 103(8), 1665–1682.

675 Page, F.Z., Kita, N.T., and Valley, J.W. (2010) Ion microprobe analysis of oxygen
676 isotopes in garnets of complex chemistry. Chemical Geology, 270(1–4), 9–19.
677 Palinkaš, S.S., Palinkaš, L.A., Renac, C., Spangenberg, J.E., Lüders, V., Molnar, F.,
678 and Maliqi, G. (2013) Metallogenic model of the Trepča Pb-Zn-Ag Skarn
679 Deposit, Kosovo: Evidence from fluid inclusions, rare earth elements, and stable
680 isotope data. Economic Geology, 108, 135–162.
681 Peng, H., Zhang, C., Mao, J., Santosh, M., Zhou, Y., and Hou, L. (2015) Garnets in
682 porphyry-skarn systems: a LA-ICP-MS, fluid inclusion, and stable isotope study
683 of garnets from the Hongniu-Hongshan copper deposit, Zhongdian area, NW
684 Yunnan province, China. Journal of Asian Earth Science, 103, 229–251.
685 Price, G.D. (1999) The evidence and implications of polar ice during the Mesozoic.
686 Earth Science Review, 48, 183–210.
687 Ramos, E.J., Hesse, M.A., Barnes, J.D., Jordan, J.S., and Lackey, J.S. (2018)
688 Reevaluating fluid sources during skarn formation: An assessment of the Empire
689 Mountain skarn, Sierra Nevada, USA. Geochemistry Geophysics Geosystems,
690 19, 3657–3672.
691 Rossetti, F., and Tecce, F. (2008) Composition and evolution of fluids during skarn
692 development in the Monte Capanne thermal aureole, Elba island, central Italy.
693 Geofluids. 8(3), 167–180.
694 Rottier, B., Kouzmanov, K., Casanova, V., Bouvier, A.S., Baumgartner, L.P., Wälle,
695 M., and Fontboté, L. (2021) Tracking fluid mixing in epithermal deposits–
696 insights from in-situ $\delta^{18}O$ and trace element composition of hydrothermal quartz
697 from the giant Cerro De Pasco polymetallic deposit, Peru. Chemical Geology,
698 576. https://doi.org/10.1016/j.chemgeo.2021.120277.
699 Russell, A.K., Kitajima, K., Strickland, A., Medaris, L.G., Schulze, D.J., and Valley,

J.W. (2013) Eclogite-facies fluid infiltration: Constraints from $\delta^{18}O$ zoning in garnet. Contribution to Mineralogy and Petrology, 165(1), 103–116.

Ryan-Davis, J., Lackey, J. S., Gevedon, M., Barnes, J.D., Lee, C.T.A., Kitajima, K., and Valley, J. (2019) Andradite skarn garnet records of exceptionally low δ18O values within an early Cretaceous hydrothermal system, Sierra Nevada, Ca. Contributions to Mineralogy & Petrology, 174(8), 68.

Samson, I.M., Williams-Jones A.E., Ault, K.M., Gagnon, J.E., and Fryer, B.J. (2008) Source of fluids forming distal Zn-Pb-Ag skarns: Evidence from laser ablation-inductively coupled plasma-mass spectrometry analysis of fluid inclusions from E1Mochito, Honduras. Geology. 36(12), 947–950.

Schwinn, G., Wagner, T., Baatartsogt, B., and Markl, G. (2006) Quantification of mixing processes in ore-forming hydrothermal systems by combination of stable isotope and fluid inclusion analyses. Geochimica Et Cosmochimica Acta, 70, 965–982.

Sharp, Z.D., and Kirschner, D. L. (1994) Quartz-calcite oxygen isotope thermometry: a calibration based on natural isotopic variations. Geochimica Et Cosmochimica Acta, 58(20), 4491–4501.

Shelton, K.L. (1983) Composition and origin of ore-forming fluids in a carbonate-hosted porphyry copper and skarn deposit: A fluid inclusion and stable isotope study of Mines Gaspe, Quebec. Economic Geology, 78, 387–421.

Sheng, J.F., and Fu, X.Z. (1999) Metallogenetic Environment and Geological Characteristics of Copper-Polymetallic Ore Deposits in Middle Part of Da Hinggan Mts. Seismological Publication House, Beijing (in Chinese).

Shi, Y.H. (2016) Petrology and zircon U-Pb geochronology of metamorphic massifs around the middle segment of the Tan-Lu fault to define the boundary between

the North and South China blocks. Journal of Asian Earth Science, http://dx.doi.org/10.1016/j.jseaes.2016.07.001.

Shu Q.H., Lai Y., Wei L.M., Sun Y., and Wang C. (2011) Fluid inclusion study of the Baiyinnuo'er Zn-Pb deposit, south segment of the Great Xing'an Mountain, northeastern China. Acta Petrologica Sinica, 27(5), 1467–1482 (in Chinese with English abstract).

Shu, Q.H., Chang, Z.S, Hammerli, J., Lai, Y., and Huizenga, J.M. (2017) Composition and evolution of fluids forming the Baiyinnuo'er Zn-Pb skarn deposit, northeastern China: insights from laser ablation ICP-MS study of fluid inclusions. Economic Geology, 112(6), 1441–1460.

Shu, Q.H., Chang, Z.S., and Mavrogenes, J. (2021) Fluid compositions reveal fluid nature, metal deposition mechanisms, and mineralization potential: An example at the Haobugao Zn-Pb skarn, China. Geology, http://doi.org/10.1130/G48348.1.

Singoyi, B., and Zaw, K. (2001) A petrological and fluid inclusion study of magnetite-scheelite skarn mineralization at Kara, Northwestern Tasmania: Implications for ore genesis. Chemical Geology, 173, 239–253.

Spicuzza, M. J., Valley, J. W., Kohn, M. J., Girard, J. P., and Fouillac, A. M. (1998) The rapid heating, defocused beam technique: a CO2-laser-based method for highly precise and accurate determination of $\delta^{18}O$ values of quartz. Chemical Geology, 144(3–4), 195–203.

Steuber, T., Rauch, M., Masse, J.P., Graaf, J., and Malkoc, M. (2005) Low-latitude seasonality of cretaceous temperatures in warm and cold episodes. Nature, 437(7063), 1341–1344.

Tracy, R.J., Robinson, P., and Thompson, A.B. (1976) Garnet composition and zoning in the determination of temperature and pressure of metamorphism, central

Massachusetts. American Mineralogist, 61, 762–775.

Vallance, J., Fontboté, L., Chiaradia, M., Markowski, A., Schmidt, S., and Vennemann, T. (2009) Magmatic-dominated fluid evolution in the Jurassic Nambija gold skarn deposits (southeastern Ecuador). Mineralium Deposita, 44, 389–413.

Valley, J. W. (1986) Stable isotope geochemistry of metamorphic rocks. Reviews in Mineralogy and Geochemistry, 16(6), 445–489.

Valley, J.W., Kitchen, N., Kohn, M.J., Niendorf, C.R., and Spicuzza, M.J. (1995) UWG-2, a garnet standard for oxygen isotope ratios: Strategies for high precision and accuracy with laser heating. Geochimica Et Cosmochimica Acta, 59, 5223–5231.

Wan, D., Li, J., Wang, Y., Wang, K., Wang, Z., and Wei, L. (2014) Re-Os radiometric dating of molybdenite in Hongling lead-zinc polymetallic deposit, Inner Mongolia, and its significance. Earth Science-Journal of China University of Geoscience, 39(6), 687–695 (in Chinese with English Abstract).

Wang, C.Y., Li, J.F., and Wang, K.Y. (2018) Fluid inclusions, stable isotopes, and geochronology of the Haobugao lead-zinc deposit, Inner Mongolia, China. Resource Geology, 69(1), 65–84.

Wang, J.B., Wang, Y.W., and Wang, L.J. (2005) Tin-polymetallic metallogenic series in the southern part of Da Hinggan Mountains, China. Geology Prospecting, 41(6), 51–60 (in Chinese with English abstract).

Wang, X.D. (2017) Magmatism and mineralization of Ag-Pb-Zn polymetallic deposits in the Lindong district, Inner Mongolia. PhD thesis of China University of Geosciences.

Whitney, D.L., and Evans, B.W. (2010) Abbreviations for names of rock-forming

775 minerals. American Mineralogist, 95(1), 185–187.

776 Wu, F.Y., Sun, D.Y., Ge, W.C., Zhang, Y.B., Grant, M.L., Wilde, S.A., and Jahn, B.M.
777 (2011) Geochronology of the Phanerozoic granitoids in northeastern China.
778 Journal of Asian Earth Science, 41, 1–30.

779 Xiao, C.D. and Wei, Y.F. (2004) The zonation and the polymetallic mineralization of
780 skarns in eastern Inner Mongolia (EIM). Geological Survey and Research,
781 27(B12), 9–15 (in Chinese with English abstract).

782 Yang, W.B., Niu, H.C., Sun, W.D., Shan, Q., Zheng, Y.F., Li, N.B., Li, C.Y., Arndt,
783 N.T., Xu, X., and Jiang, Y.H. (2013) Isotopic evidence for continental ice sheet in
784 mid-latitude region in the supergreenhouse Early Cretaceous. Scientific Reports,
785 3, 2732. DOI:10.1038/srep02732.

786 Zhang, L.G., Liu, J.X., Chen, Z.S., and Zhou, H.B. (1994) Experimental
787 investigations of oxygen isotope fractionation in cassiterite and wolframite.
788 Economic Geology, 89, 150–157.

789 Zhao, Y.M., Wang, D.W., Zhang, D.Q., Fu, X.Z., Bao, X.P., Li, H.N., and Ai, Y.F.
790 (1994) Ore controlling factors and ore-prospecting models for copper
791 polymetallic deposits in southeast Inner Mongolia. Seismological Press, Beijing.
792 234 (in Chinese).

793 Zhao X.Y., Zheng Y.C., Yang Z.S., and Hu Li. (2020) Formation and evolution of
794 multistage ore-forming fluids in the Miocene Bangpu porphyry–skarn deposit,
795 Southern Tibet: Insights from LA–ICP–MS trace elements of quartz and fluid
796 inclusions. Journal of Asian Earth Science, 204,
797 https://doi.org/10.1016/j.jseaes.2020.104556.

798 Zheng, Y.F. (1993a) Calculation of oxygen isotope fractionation in hydroxyl-bearing
799 silicates. Earth and Planetary Science Letters, 210, 247–263.

Zheng, Y.F. (1993b) Calculation of oxygen isotope fractionation in anhydrous silicate minerals. Geochimica Et Cosmochimica Acta, 57(5), 1079–1091.

Zhong, S.T., Feng, C.Y., Seltmann, R., Dolgopolova, A., Andersen, J., Li, D.X., and Yu, M. (2018) Sources of fluids and metals and evolution models of skarn deposits in the Qimantagh metallogenic belt: A case study from the Weibao deposit, East Kunlun Mountains, northern Tibetan Plateau. Ore Geology Reviews, 93, 19–37.

List of figure captions

Figure 1. a. Simplified geotectonic map of northeastern China with the location of the Haobugao Zn-Fe-Sn deposit (after Wu et al., 2011), b. Map showing the distribution of ore deposits in the southern Great Xing'an Range (modified after Liu et al., 2018) and c. geologic map of the Haobugao skarn Zn-Fe-Sn deposit (after Wan et al., 2014)

Figure 2. Simplified geologic cross sections of drill holes ZK2510 and ZK2511, showing the spatial relationship among different strata units, intrusions, and skarn. The Pb-Zn ores occur disseminated and as veinlets in the skarn and adjacent.

Figure 3. Typical skarn hand specimens from the Haobugao deposit (after Liu et al., 2021a). (a) Diopside in exoskarn replaced by quartz-pyrite; (b) Sulfide ore consisting of diopside, sphalerite, bornite and calcite in exoskarn; (c) Massive light yellow-brown fine-grained granular garnet and pyroxene in the central exoskarn; (d) Green coarse-grained garnet overgrown by light yellow-brown fine-grained garnet in the central exoskarn; quartz-magnetite replacing garnet skarn; (e) Grossular garnet and hedenbergite pyroxene in proximal exoskarn; (f) Granite altered by chlorite in endoskarn. Grt: garnet; Cpx: clinopyroxene; Mt: magnetite; Qz: quartz; Cal: calcite; Sp: sphalerite; Bn: bornite; Chl: chlorite; Py: pyrite. Mineral abbreviations refer to Whitney and Evans (2010).

825 **Figure 4.** Paragenetic sequence of minerals from the Haobugao Zn-Fe-Sn
826 polymetallic deposit.

827 **Figure 5.** Typical hand specimens and micro photos of retrograde stage samples from
828 the Haobugao deposit. (a) Radial vesuvianite replaced by arsenopyrite and magnetite;
829 (b) Reflected light image showing vesuvianite replaced by arsenopyrite; (c) Sandstone
830 altered to hydrothermal tremolite and titanite; (d) Garnet replaced by amphibole; (e)
831 Garnet replaced by amphibole and cassiterite; (f) Skarn with magnetite replacing
832 garnet-diopside; (g) BSE image showing magnetite replacing garnet and diopside; (h);
833 Banded quartz, magnetite and sulfides ore; (i) Quartz-arsenopyrite-chalcopyrite vein
834 with brown alteration halo in tuff; (j) BSE image showing magnetite was replaced by
835 quartz, chalcopyrite, pyrite and calcite assemblage; (k) BSE image showing magnetite
836 and arsenopyrite were replaced by quartz, calcite and fluorite; (l) Diopside skarn
837 replaced by sphalerite and galena; (m) Plane-polarized light image showing brown
838 sphalerite, quartz and calcite filling between garnet crystals; (n) Subhedral quartz and
839 sphalerite and chalcopyrite grow along the garnet rim; (o) Euhedral quartz, calcite,
840 chalcopyrite, sphalerite and chlorite assemblage. Grt: garnet; Di: diopside; Ves:
841 vesuvianite; Mt: magnetite; Cst: cassiterite; Amp: amphibole; Tr: tremolite; Qz:
842 quartz; Apy: arsenopyrite; Ccp: Chalcopyrite; Ttn: titanite; Cal: calcite; Sp: sphalerite;
843 Py: pyrite; Chl: chlorite; Fl: fluorite.

844 **Figure 6.** Ternary diagram showing composition of (a) garnet, and (b) pyroxene. The
845 composition of garnet and pyroxene from other skarn ore deposits are from Meinert et
846 al. (2005). Pyr: pyrope; Grs: grossular; Adr: andradite; Jo: johannsenite; Di: diopside;
847 Hd: hedenbergite.

848 **Figure 7.** Oxygen isotopic results of individual SIMS analytical spots of garnet and
849 pyroxene versus depth.

Figure 8. $\delta^{18}O$ values of individual garnets from central zone exoskarn. (a) sample ZK2510-369; (b) sample ZK2511-438; (c) sample ZK2510-468; (d) sample ZK2511-454; (e) sample ZK2510-468; (f) sample ZK2511-423. The colored panels within the plots indicates different domains (core-mantle-rim) of the garnets. The red circles are the position of SIMS spots. The pits in 8c are previous LA-ICP-MS spots which were preserved. T (°C) is calculated isotope equilibrium temperature of garnet and pyroxene. The variation of T are attributed to the variation (within 2S.D., 0.6‰) of $\delta^{18}O$ in the crystal.

Figure 9. Micrographs of pyroxene from distal exoskarn and $\delta^{18}O$ values displayed in BSE images. (a) Sample ZK2510-29 showing early diopside replaced by hedenbergite, following by quartz and sphalerite alteration; (b) Early diopside with high $\delta^{18}O$ values replaced by hedenbergite with lower $\delta^{18}O$ values; (c) Sample Zk2511-79 showing hedenbergite altered by quartz and pyrite; (d) BSE image showing hedenbergite with homogeneous low $\delta^{18}O$ values. Hd: hedenbergite; Di: diopside; Qz: quartz; Ccp: chalcopyrite; Sp: sphalerite; Py: pyrite; An: anorthite.

Figure 10. $\delta^{18}O_{fluid}$ of minerals from different stages of the Haobugao skarn deposit. The garnets and pyroxenes in the outlined early skarn stage are separated according to the mineral growth sequence. The blue line indicates the evolution trend of $\delta^{18}O_{fluid}$.

Figure 11. Schematic hydrothermal fluid evolution model for the Haobugao skarn system. (A) Early skarn stage, different generations of garnet and diopside were formed with the magmatic water, meteoric water and metamorphic water, and no mineralization occurred; (b) Late skarn stage, hedenbergite and hydrous minerals, such as vesuvianite, formed, accompanied by a small amount of cassiterite; (c) Oxide stage, with the addition of meteoric water, magnetite precipitates and replaces the early skarn minerals; (d) Quartz-sulfide stage, with the input of a large amount of

meteoric water, the decrease of temperature and the decomposition of the complex, high-temperature minerals such as chalcopyrite, molybdenite and arsenopyrite precipitate first, followed by massive precipitation of sphalerite, galena and calcite. Adr: andradite; Grs: grossular; Di: diopside; Hd: hedenbergite; Ves: vesuvianite; Cst: cassiterite; Mt: magnetite. The gray background is siltstone.

List of table captions

Table 1. In-situ oxygen isotopic analysis result of garnet in the Haobugao deposit.

Table 2. In-situ oxygen isotopic analysis result of pyroxene in the Haobugao deposit.

Table 3. In-situ oxygen isotopic analysis results of vesuvianites and tremolites in the Haobugao deposit.

Table 4. In-situ oxygen isotopic analysis result of cassiterite in the Haobugao deposit.

Table 5. In-situ oxygen isotopic analysis results of quartz and calcite in the Haobugao deposit.

Table S1. EMPA data of pyroxenes in the Haobugao deposit. On the basis of 6 oxygen atoms and 4 cations.

Table S2. Oxygen isotopic results of hedenbergite, tremolite and vesuvianite obtained by laser fluorination analyses.

This is the peer-reviewed, final accepted version for American Mineralogist, published by the Mineralogical Society of America.
The published version is subject to change. Cite as Authors (Year) Title. American Mineralogist, in press.
DOI: https://doi.org/10.2138/am-2022-8523. http://www.minsocam.org/

Table 1

Mineral	Sample	Mount_Sample_ Grain.Analysis	Domin	^{16}O (CPS)	Raw $^{18}O/^{16}O$ Ratio	±2s	$\delta^{18}O$ (‰, VSMOW)	IMF (‰)	$\delta^{18}O$ (‰, VSMOW) ME corr	±2s (internal)	±2s (external)	X_{Grs}	X_{Prp}	X_{alm}	X_{Sps}	X_{adr}	Temperature (℃)	Fractionation factor (‰)	$\delta^{18}O_{fluid}$ (‰,VSMOW)	Fractionation factor (‰, +50℃/-50℃)	Error of $\delta^{18}O_{fluid}$ (‰,VSMOW, +50℃/-50℃)
Garnet	Zk2510-369	Z6844_10_Grt_1.1	core	2.37E+09	0.002021537	2.74E-07	9.2	6.8	2.4	0.1	0.6	0.04	0.01	0.00	0.01	0.95	500	-2.9	5.3	-2.9/-2.8	0/-0.1
Garnet	Zk2510-369	Z6844_10_Grt_1.2	core	2.28E+09	0.002023297	1.69E-07	10.1	6.8	3.3	0.1	0.6	0.04	0.01	0.00	0.01	0.95	500	-2.9	6.2	-2.9/ -2.8	0/-0.1
Garnet	Zk2510-369	Z6844_10_Grt_1.3	core	2.29E+09	0.002023453	1.92E-07	10.2	6.7	3.4	0.1	0.6	0.05	0.01	0.00	0.01	0.93	500	-2.9	6.3	-2.9/ -2.8	0/-0.1
Garnet	Zk2510-369	Z6844_10_Grt_1.4	core	2.33E+09	0.002022876	4.34E-07	9.9	6.7	3.1	0.2	0.6	0.05	0.01	0.00	0.01	0.93	500	-2.9	6.0	-2.9/ -2.8	0/-0.1
Garnet	Zk2510-369	Z6844_10_Grt_1.5	rim	2.18E+09	0.002021055	2.59E-07	9.0	6.7	2.3	0.1	0.6	0.10	0.01	0.00	0.01	0.89	500	-2.9	5.2	-2.9/ -2.8	0/-0.1
Garnet	Zk2510-369	Z6844_10_Grt_1.6	rim	2.10E+09	0.002021416	2.15E-07	9.2	6.2	2.9	0.1	0.6	0.29	0.00	0.00	0.01	0.70	500	-2.9	5.8	-2.9/ -2.8	0/-0.1
Garnet	Zk2510-369	Z6844_10_Grt_1.7	rim	2.14E+09	0.002019579	2.30E-07	8.2	6.2	2.0	0.1	0.6	0.29	0.01	0.00	0.01	0.69	500	-2.9	4.9	-2.9/ -2.8	0/-0.1
Garnet	Zk2510-369	Z6844_10_Grt_1.8	rim	2.21E+09	0.002015574	2.14E-07	6.2	6.0	0.3	0.1	0.6	0.36	0.00	0.00	0.01	0.63	500	-2.9	3.2	-2.9/ -2.8	0/-0.1
Garnet	ZK2511-869	Z6844_8_Grt_1.1		2.22E+09	0.002022510	2.42E-07	9.7	5.0	4.7	0.1	0.6	0.49	0.00	0.04	0.01	0.46	500	-3.0	7.7	-3.0/ -2.9	0/-0.1
Garnet	ZK2511-869	Z6844_8_Grt_1.2		2.21E+09	0.002021998	3.62E-07	9.4	4.8	4.7	0.2	0.6	0.54	0.00	0.04	0.01	0.42	500	-3.0	7.7	-3.0/ -2.9	0/-0.1
Garnet	ZK2511-869	Z6844_8_Grt_1.3		2.20E+09	0.002022531	2.27E-07	9.7	5.1	4.6	0.1	0.6	0.47	0.00	0.05	0.01	0.48	500	-3.0	7.6	-3.0/ -2.9	0/-0.1
Garnet	ZK2511-869	Z6844_8_Grt_1.4		2.22E+09	0.002021806	1.99E-07	9.4	5.2	4.1	0.1	0.6	0.47	0.00	0.03	0.01	0.49	500	-3.0	7.1	-3.0/ -2.9	0/-0.1
	Standard																				
	UWG2 Garnet (average, n=24 out of 27)			2.09E+09	0.002014683	1.20E-06	5.8	0.0	5.8		0.6										
	GRS-2 Grt (average, n=5)			2.08E+09	0.002023098	5.74E-07	10.0	2.0	8.0		0.3										
	AND-RG Grt (average, n=5)			2.42E+09	0.002025795	5.60E-07	11.3	7.0	4.4		0.3										
Garnet	Zk2511-438	Z6910_2_Grt_1.1	core	1.95E+09	0.002014366	2.85E-07	7.8	6.8	1.1	0.1	0.6	0.01	0.01	0.00	0.01	0.97	500	-2.9	4.0	-2.9/ -2.8	0/-0.1
Garnet	Zk2511-438	Z6910_2_Grt_1.2	core	2.10E+09	0.002007340	5.18E-07	4.3	6.8	-2.5	0.3	0.6	0.01	0.01	0.00	0.01	0.97	500	-2.9	0.4	-2.9/ -2.8	0/-0.1
Garnet	Zk2511-438	Z6910_2_Grt_1.3	core	1.07E+09	0.002019392	3.11E-07	10.4	6.2	4.1	0.2	0.6	0.30	0.00	0.00	0.01	0.69	500	-2.9	7.0	-2.9/ -2.8	0/-0.1
Garnet	Zk2511-438	Z6910_2_Grt_1.4	core	1.98E+09	0.002014594	1.75E-07	8.0	6.7	1.3	0.1	0.6	0.04	0.01	0.00	0.01	0.94	500	-2.9	4.2	-2.9/ -2.8	0/-0.1
Garnet	Zk2511-438	Z6910_2_Grt_1.5	rim	2.21E+08	0.002022762	8.45E-07	12.0	6.1	6.0	0.4	0.7	0.32	0.00	0.01	0.01	0.66	500	-2.9	8.9	-2.9/ -2.8	0/-0.1
Garnet	Zk2511-438	Z6910_2_Grt_1.6	rim	4.98E+08	0.002021720	2.37E-07	11.5	6.1	5.4	0.1	0.6	0.32	0.00	0.01	0.01	0.66	500	-2.9	8.3	-2.9/ -2.8	0/-0.1
Garnet	Zk2511-438	Z6910_2_Grt_1.7	rim	1.97E+09	0.002016250	3.27E-07	8.8	6.8	2.0	0.2	0.6	0.03	0.01	0.00	0.01	0.95	500	-2.9	4.9	-2.9/ -2.8	0/-0.1
Garnet	Zk2511-438	Z6910_2_Grt_1.8	rim	1.74E+09	0.002015443	1.15E-07	8.4	6.8	1.6	0.1	0.6	0.03	0.01	0.00	0.01	0.95	500	-2.9	4.5	-2.9/ -2.8	0/-0.1
Garnet	Zk2511-438	Z6910_2_Grt_1.9	rim	1.91E+09	0.002015791	2.48E-07	8.6	6.0	2.5	0.1	0.6	0.34	0.00	0.00	0.01	0.65	500	-2.9	5.4	-2.9/ -2.8	0/-0.1
Garnet	ZK2511-454	Z6910_5_Grt_1.1	core	1.96E+09	0.002013176	1.08E-07	7.2	6.8	0.5	0.1	0.6	0.02	0.01	0.00	0.01	0.97	500	-2.9	3.4	-2.9/ -2.8	0/-0.1
Garnet	ZK2511-454	Z6910_5_Grt_1.2	core	1.91E+09	0.002012302	1.24E-07	6.8	6.7	0.1	0.1	0.6	0.12	0.00	0.00	0.01	0.87	500	-2.9	3.0	-2.9/ -2.8	0/-0.1
Garnet	ZK2511-454	Z6910_5_Grt_1.3	rim	1.75E+09	0.002010078	3.54E-07	5.7	6.8	-1.1	0.2	0.6	0.02	0.01	0.00	0.01	0.97	500	-2.9	1.8	-2.9/ -2.8	0/-0.1

Garnet	ZK2511-454	Z6910_5_Grt_1.4	rim	1.83E+09	0.002006063	1.77E-07	3.7	6.6	-2.9	0.1	0.6	0.14	0.00	0.00	0.01	0.84	500	-2.9	0.0	-2.9/ -2.8	0/-0.1
Garnet	ZK2511-454	Z6910_5_Grt_1.5	rim	1.91E+09	0.002004267	1.87E-07	2.8	6.6	-3.8	0.1	0.6	0.14	0.00	0.00	0.01	0.84	500	-2.9	-0.9	-2.9/ -2.8	0/-0.1
		Z6910_5_Grt_1.5																			
Garnet	ZK2511-454	B	rim	1.88E+09	0.002005997	1.97E-07	3.7	6.6	-3.0	0.1	0.6	0.14	0.00	0.00	0.01	0.84	500	-2.9	-0.1	-2.9/ -2.8	0/-0.1
Garnet	ZK2511-454	Z6910_5_Grt_1.6	rim	1.89E+09	0.002004764	1.55E-07	3.0	6.7	-3.7	0.1	0.6	0.04	0.01	0.00	0.01	0.94	500	-2.9	-0.8	-2.9/ -2.8	0/-0.1
Garnet	ZK2511-454	Z6910_5_Grt_1.7	rim	1.71E+09	0.002008678	3.46E-07	5.0	6.7	-1.7	0.2	0.6	0.02	0.01	0.00	0.01	0.96	500	-2.9	1.2	-2.9/ -2.8	0/-0.1
Garnet	ZK2511-454	Z6910_5_Grt_1.8	rim	1.66E+09	0.002008859	2.00E-07	5.1	6.6	-1.5	0.1	0.6	0.14	0.00	0.00	0.01	0.84	500	-2.9	1.4	-2.9/ -2.8	0/-0.1
Garnet	ZK2511-454	Z6910_5_Grt_1.9	rim	1.64E+09	0.002010832	1.27E-07	6.1	6.8	-0.7	0.1	0.6	0.03	0.00	0.00	0.01	0.95	500	-2.9	2.2	-2.9/ -2.8	0/-0.1
Garnet	ZK2511-454	Z6910_5_Grt_1.10	rim	1.60E+09	0.002012336	1.65E-07	6.8	6.4	0.4	0.1	0.6	0.22	0.01	0.00	0.01	0.76	500	-2.9	3.3	-2.9/ -2.8	0/-0.1
Garnet	ZK2511-454	Z6910_5_Grt_1.11	rim	1.61E+09	0.002014355	1.12E-07	7.8	6.1	1.7	0.1	0.6	0.31	0.00	0.01	0.01	0.67	500	-2.9	4.6	-2.9/ -2.8	0/-0.1
Garnet	ZK2510-468-1	Z6911_6_Grt_1.1	core	1.83E+09	0.002012620	2.26E-07	7.0	5.6	1.4	0.1	0.6	0.44	0.00	0.00	0.01	0.55	500	-3.0	4.4	-3.0/ -2.9	0/-0.1
Garnet	ZK2510-468-1	Z6911_6_Grt_1.2	core	1.76E+09	0.002012743	1.28E-07	7.0	5.3	1.7	0.1	0.6	0.47	0.00	0.00	0.02	0.50	500	-3.0	4.7	-3.0/ -2.9	0/-0.1
Garnet	ZK2510-468-1	Z6911_6_Grt_1.3	rim	1.70E+09	0.002007852	1.15E-07	4.6	3.2	1.4	0.1	0.6	0.76	0.00	0.03	0.02	0.19	500	-3.0	4.4	-3.0/ -2.9	0/-0.1
Garnet	ZK2510-468	Z6911_7_Grt_1.1	core	1.79E+09	0.001997336	1.59E-07	-0.7	5.5	-6.2	0.1	0.6	0.45	0.00	0.00	0.01	0.54	500	-3.0	-3.2	-3.0/ -2.9	0/-0.1
Garnet	ZK2510-468	Z6911_7_Grt_1.2	core	1.79E+09	0.001998108	2.69E-07	-0.3	5.9	-6.1	0.1	0.6	0.36	0.00	0.01	0.01	0.61	500	-3.0	-3.1	-3.0/ -2.9	0/-0.1
Garnet	ZK2510-468	Z6911_7_Grt_1.3	rim	1.81E+09	0.001993311	1.70E-07	-2.7	5.4	-8.1	0.1	0.6	0.47	0.00	0.00	0.02	0.51	500	-3.0	-5.1	-3.0/ -2.9	0/-0.1
Garnet	ZK2510-468	Z6911_7_Grt_1.4	vein	1.79E+09	0.002013563	2.62E-07	7.4	5.5	1.9	0.1	0.6	0.41	0.00	0.02	0.02	0.55	500	-3.0	4.8	-3.0/ -2.9	0/-0.1
Garnet	ZK2510-468	Z6911_7_Grt_1.5	core	1.95E+09	0.002014708	2.26E-07	8.0	6.8	1.2	0.1	0.6	0.03	0.00	0.00	0.01	0.95	500	-3.0	4.1	-3.0/ -2.9	0/-0.1
Garnet	ZK2510-468	Z6911_7_Grt_1.6	core	1.94E+09	0.002014510	4.36E-07	7.9	6.8	1.1	0.2	0.6	0.01	0.00	0.00	0.01	0.98	500	-3.0	4.0	-3.0/ -2.9	0/-0.1
Garnet	ZK2510-468	Z6911_7_Grt_1.7	core	1.96E+09	0.002012603	2.51E-07	7.0	6.8	0.2	0.1	0.6	0.02	0.00	0.00	0.01	0.96	500	-3.0	3.1	-3.0/ -2.9	0/-0.1
Garnet	ZK2510-468	Z6911_7_Grt_1.8	core	1.84E+09	0.002011852	2.44E-07	6.6	6.8	-0.2	0.1	0.6	0.02	0.00	0.00	0.01	0.96	500	-3.0	2.7	-3.0/ -2.9	0/-0.1
Garnet	ZK2510-468	Z6911_7_Grt_1.9	rim	1.72E+09	0.002013917	2.85E-07	7.6	5.6	2.0	0.1	0.6	0.39	0.00	0.01	0.03	0.57	500	-3.0	4.9	-3.0/ -2.9	0/-0.1
Garnet	ZK2510-468	Z6911_7_Grt_1.10	rim	1769895450	0.002009863	3.55E-07	5.6	5.8	-0.2	0.2	0.6	0.36	0.00	0.00	0.03	0.60	500	-3.0	2.7	-3.0/ -2.9	0/-0.1
Garnet	ZK2511-423	Z6911_9_Grt_1.1		1.89E+09	0.002020277	2.35E-07	10.8	5.3	5.5	0.1	0.6	0.50	0.00	0.00	0.01	0.49	500	-3.0	8.4	-3.0/ -2.9	0/-0.1
Garnet	ZK2511-423	Z6911_9_Grt_1.2		1.88E+09	0.002019355	3.20E-07	10.3	5.4	5.0	0.2	0.6	0.48	0.00	0.00	0.01	0.51	500	-3.0	7.9	-3.0/ -2.9	0/-0.1
Garnet	ZK2511-423	Z6911_9_Grt_1.3		1.85E+09	0.002020676	3.13E-07	11.0	5.4	5.6	0.2	0.6	0.48	0.00	0.00	0.01	0.51	500	-3.0	8.5	-3.0/ -2.9	0/-0.1
	Standard																				
	UWG2 Garnet (average,																				
	n=43 out of 50)			1.67E+09	0.002010289	1.16E-06	5.8	0.0	5.8		0.6										
	ANDRG Garnet (average,																				
	n=5)			2.03E+09	0.002019620	2.05E-06	10.5	6.1	4.4		1.0										
	GRS2 Garnet (average, n=5)			1.72E+09	0.002017433	1.16E-06	9.4	1.4	8.0		0.6										

This is the peer-reviewed, final accepted version for American Mineralogist, published by the Mineralogical Society of America.
The published version is subject to change. Cite as Authors (Year) Title. American Mineralogist, in press.
DOI: https://doi.org/10.2138/am-2022-8523. http://www.minsocam.org/

Table 2

Mineral	Sample	Mount_Sample_Grain .Analysis	Raw ^{16}O (CPS)	Raw $^{18}O/^{16}O$ Ratio	±2s	$\delta^{18}O$ (‰, VSMOW)	IMF (‰)	$\delta^{18}O$ (‰, VSMOW) ME corr	±2s (internal)	±2s (external)	Xwo	Xen	XFs	Temperature (°C)	Fractionation factor (%)	$\delta^{18}O_{fluid}$ (‰,VSMOW)	Fractionation factor (‰, +50°C/-50°C)	Error of $\delta^{18}O_{fluid}$ (‰,VSMOW, +50°C/-50°C)
Pyroxene	Zk2511-470	Z6844_11_Di_1.1	2.12E+09	0.002017468	2.22E-07	4.3	0.1	4.3	0.1	0.6	50.94	39.60	9.46	500	-1.9	6.2	-2.1/ -1.8	+0.2/ -0.1
Pyroxene	Zk2511-470	Z6844_11_Di_1.2	2.12E+09	0.002017883	2.99E-07	4.6	0.7	3.9	0.1	0.6	51.07	36.26	12.67	500	-1.9	5.8	-2.1/ -1.8	+0.2/ -0.1
Pyroxene	Zk2511-470	Z6844_11_Di_1.3	2.11E+09	0.002016460	2.65E-07	3.8	0.3	3.6	0.1	0.6	51.04	38.54	10.42	500	-1.9	5.5	-2.1/ -1.8	+0.2/ -0.1
		869 Hd (average, n=4)	2.21E+09	0.002018964	5.22E-06			0.3		2.6								
Pyroxene	ZK2511-869	Z6844_9_869_Hd_1.1	2.22E+09	0.002020514	1.95E-07	5.9	6.5	-0.6	0.1	0.6	50.84	5.07	44.09	500	-1.9	1.3	-2.0/ -1.7	+0.1/ -0.2
Pyroxene	ZK2511-869	Z6844_9_869_Hd_1.2	2.21E+09	0.002022254	2.63E-07	6.7	5.8	0.9	0.1	0.6	50.82	8.76	40.42	500	-1.9	2.8	-2.0/ -1.7	+0.1/ -0.2
Pyroxene	ZK2511-869	Z6844_9_869_Hd_1.3	2.20E+09	0.002023362	3.58E-07	7.3	6.0	1.3	0.2	0.6	51.12	7.74	41.15	500	-1.9	3.2	-2.0/ -1.7	+0.1/ -0.2
Pyroxene	ZK2511-869	Z6844_9_869_Hd_1.4	2.21E+09	0.002022739	1.85E-07	7.0	5.9	1.1	0.1	0.6	50.86	8.29	40.85	500	-1.9	3.0	-2.0/ -1.7	+0.1/ -0.2
	Standard																	
	UWC3 Di (average, n=13)		2.10E+09	0.002029179	1.26E-06	10.2	0.0	10.2		0.6								
	NRM-AG1 Cpx (average, n=7)		2.15E+09	0.002021124	1.24E-06	6.2	0.7	5.5		0.6								
Pyroxene	Zk2511-438	Z6910_1_Di_1.1	1.72E+09	0.002007546	2.41E-07	2.1	-0.7	2.7	0.1	0.6	50.70	43.90	5.40	500	-1.9	4.6	-2.1/ -1.8	+0.2/ -0.1
Pyroxene	Zk2511-438	Z6910_1_Di_1.2	1.71E+09	0.002011053	2.39E-07	3.8	-0.7	4.5	0.1	0.6	50.70	43.90	5.40	500	-1.9	6.4	-2.1/ -1.8	+0.2/ -0.1
Pyroxene	Zk2511-438	Z6910_1_Di_1.3	1.66E+09	0.002009822	2.75E-07	3.2	-0.7	3.9	0.1	0.6	50.70	43.90	5.40	500	-1.9	5.8	-2.1/ -1.8	+0.2/ -0.1
Pyroxene	ZK2510-468	Z6911_6_Di_1.1	1.74E+09	0.002012149	2.86E-07	4.4	0.7	3.7	0.1	0.6	50.80	36.59	12.61	500	-1.9	5.6	-2.1/ -1.8	+0.2/ -0.1
Pyroxene	ZK2510-468	Z6911_6_Di_2.1	1.72E+09	0.002010375	2.31E-07	3.5	-0.1	3.6	0.1	0.6	50.95	40.69	8.36	500	-1.9	5.5	-2.1/ -1.8	+0.2/ -0.1
Pyroxene	ZK2510-468	Z6911_7_Di_1.1	1.70E+09	0.002010364	9.20E-08	3.5	-0.7	4.1	0.0	0.6	50.70	43.90	5.40	500	-1.9	6.0	-2.1/ -1.8	+0.2/ -0.1
Pyroxene	ZK2510-468	Z6911_7_Di_1.2	1.70E+09	0.002011646	1.83E-07	4.1	-0.7	4.8	0.1	0.6	50.70	43.90	5.40	500	-1.9	6.7	-2.1/ -1.8	+0.2/ -0.1
Pyroxene	ZK2511-423	Z6911_9_Di_1.1	1.77E+09	0.002015964	1.97E-07	6.3	1.3	5.0	0.1	0.6	51.07	32.94	15.99	500	-1.9	6.9	-2.1/ -1.8	+0.2/ -0.1
Pyroxene	ZK2511-423	Z6911_9_Di_2.1	1.76E+09	0.002016111	3.68E-07	6.3	1.3	5.0	0.2	0.6	51.37	32.65	15.98	500	-1.9	6.9	-2.1/ -1.8	+0.2/ -0.1
	Standard																	
	97DL65 Diopside (average,		1.62E+09	0.002012035	1.20E-06	4.3	-0.9	5.2		0.6								

	n=15)																	
	UWC3 Diopside (average, n=5)		1.55E+09	0.002023795	9.21E-07	10.2	0.0	10.2		0.5								
Pyroxene	ZK2510-29	Z6970_29_Di_1.1	1.23E+09	0.002016009	1.29E-07	5.6	-0.7	6.3	0.1	0.1	51.51	43.08	5.42	500	-1.9	8.2	-2.1/ -1.8	+0.2/ -0.1
Pyroxene	ZK2510-29	Z6970_29_Di_1.2	1.25E+09	0.002016074	4.00E-07	5.7	-0.7	6.3	0.2	0.2	51.51	43.08	5.42	500	-1.9	8.2	-2.1/ -1.8	+0.2/ -0.1
Pyroxene	ZK2510-29	Z6970_29_Hd_1.1	1.25E+09	0.002014731	3.32E-07	5.0	4.1	0.9	0.2	0.2	51.26	17.40	31.34	500	-1.9	2.8	-2.0/ -1.7	+0.1/ -0.2
Pyroxene	ZK2510-29	Z6970_29_Hd_1.2	1.23E+09	0.002018545	4.23E-07	6.9	3.5	3.4	0.2	0.2	51.08	20.87	28.05	500	-1.9	5.3	-2.0/ -1.7	+0.1/ -0.2
Pyroxene	ZK2510-29	Z6970_29_Hd_1.3	1.27E+09	0.002015804	4.45E-07	5.5	4.0	1.6	0.2	0.2	51.23	18.39	30.38	500	-1.9	3.5	-2.0/ -1.7	+0.1/ -0.2
Pyroxene	ZK2510-79	Z6970_31_Hd_1.1	1.25E+09	0.002021734	2.19E-07	8.5	5.6	2.9	0.1	0.1	49.83	10.90	39.27	500	-1.9	4.8	-2.0/ -1.7	+0.1/ -0.2
Pyroxene	ZK2510-79	Z6970_31_Hd_1.2	1.26E+09	0.002021085	2.97E-07	8.2	5.6	2.6	0.1	0.2	49.83	10.90	39.27	500	-1.9	4.5	-2.0/ -1.7	+0.1/ -0.2
Pyroxene	ZK2510-79	Z6970_31_Hd_2.1	1.26E+09	0.002021122	2.02E-07	8.2	5.6	2.6	0.1	0.1	49.83	10.90	39.27	500	-1.9	4.5	-2.0/ -1.7	+0.1/ -0.2
Pyroxene	ZK2510-79	Z6970_31_Hd_2.2	1.25E+09	0.002020806	3.53E-07	8.0	5.6	2.4	0.2	0.2	49.83	10.90	39.27	500	-1.9	4.3	-2.0/ -1.7	+0.1/ -0.2
Pyroxene	ZK2510-79	Z6970_31_Hd_2.3	1.25E+09	0.002020403	4.01E-07	7.8	5.6	2.2	0.2	0.2	49.83	10.90	39.27	500	-1.9	4.1	-2.0/ -1.7	+0.1/ -0.2
	Standard																	
	UWC3 (or 95AK24) Diopside																	
	(average, n=5)		1.21E+09	0.002025099	1.22E-06	10.2	0.0	10.2		0.6								
	97SL65 Diopside (average,																	
	n=14)		1.20E+09	0.002012167	9.54E-07	3.7	-1.5	5.2		0.5								
	869 Hd (average, n=4 out of 6)		1.25E+09	0.002017927	9.20E-07	6.6	6.3	0.3		0.5								
	NRM-AG1 Cpx (average, n=5)		1.24E+09	0.002016905	3.62E-07	6.1	0.6	5.5		0.2								

This is the peer-reviewed, final accepted version for American Mineralogist, published by the Mineralogical Society of America.
The published version is subject to change. Cite as Authors (Year) Title. American Mineralogist, in press.
DOI: https://doi.org/10.2138/am-2022-8523. http://www.minsocam.org/

Table 3

Mineral	Sample	Mount_Sample_Grain.Analysis	^{16}O (CPS)	Raw $^{18}O/^{16}O$ Ratio	±2s	$\delta^{18}O$ (‰, VSMOW)	IMF (‰)	$\delta^{18}O$ (‰, VSMOW) ME corr	±2s (internal)	±2s (external)	Temperature (°C)	Fractionation factor (%)	$\delta^{18}O_{fluid}$ (‰,VSMOW)	Fractionation factor (‰, +50°C/-50°C)	Error of $\delta^{18}O_{fluid}$ (‰,VSMOW, +50°C/-50°C)
Vesuvianite	ZK1708-623	Z6843_2_Ves_1.1	2.00E+09	0.00202126	0.000000218			4.2	0.1	0.6	450	-4.1	8.3	-4.0/ -4.0	+0.1/ +0.1
Vesuvianite	ZK1708-623	Z6843_2_Ves_1.2	2.03E+09	0.002019522	0.000000448			3.4	0.2	0.6	450	-4.1	7.5	-4.0/ -4.0	+0.1/ +0.1
Vesuvianite	ZK1708-623	Z6843_2_Ves_1.3	2.02E+09	0.002020736	0.000000263			4.0	0.1	0.6	450	-4.1	8.1	-4.0/ -4.0	+0.1/ +0.1
Vesuvianite	ZK1708-618	Z6843_3_Ves_1.1	1.96E+09	0.002020306	0.00000027			3.7	0.1	0.6	450	-4.1	7.8	-4.0/ -4.0	+0.1/ +0.1
Vesuvianite	ZK1708-618	Z6843_3_Ves_1.2	2.00E+09	0.00202072	0.000000221			4.0	0.1	0.6	450	-4.1	8.1	-4.0/ -4.0	+0.1/ +0.1
Vesuvianite	ZK1708-618	Z6843_3_Ves_1.3	1.91E+09	0.002021593	0.000000239			4.4	0.1	0.6	450	-4.1	8.5	-4.0/ -4.0	+0.1/ +0.1
	ZK1708-618 Vesuvianite (average, n=6)		1.99E+09	2.02E-03	1.4574E-06			3.9		0.7					
Tremolite	Zk2511-162	Z6843_4_Tre_1.1	2.07E+09	0.002021879	0.000000238			5.7	0.1	0.6	450	-1.5	7.2	-1.7/ -1.2	+0.2/ -0.3
Tremolite	Zk2511-162	Z6843_4_Tre_1.2	2.01E+09	0.002022709	0.000000343			6.1	0.2	0.6	450	-1.5	7.6	-1.7/ -1.2	+0.2/ -0.3
Tremolite	Zk2511-162	Z6843_4_Tre_1.3	2.12E+09	0.002021073	0.000000233			5.3	0.1	0.6	450	-1.5	6.8	-1.7/ -1.2	+0.2/ -0.3
	ZK2511-13-162 Tremolite (average, n=3)		2.07E+09	2.02E-03	1.63606E-06			5.7		0.8					
	Standard														
	UWC3 Di (average, n=13)		2.10E+09	2.03E-03	1.26402E-06	13.0	-2.8	10.2		0.6					
	NRM-AG1 Cpx (average, n=7)		2.15E+09	2.02E-03	1.23879E-06	9.0	-3.5	5.5		0.6					

This is the peer-reviewed, final accepted version for American Mineralogist, published by the Mineralogical Society of America.
The published version is subject to change. Cite as Authors (Year) Title. American Mineralogist, in press.
DOI: https://doi.org/10.2138/am-2022-8523. http://www.minsocam.org/

Table 4

Mineral	Mount_Sample_Grain.Analysis	^{16}O (CPS)	Raw $^{18}O/^{16}O$ Ratio	±2s	$\delta^{18}O$ (‰, VSMOW)	±2s (internal)	±2s (external)	Temperature (℃)	Fractionation factor (‰)	$\delta^{18}Ofluid$ (‰, VSMOW)	Fractionation factor (‰, +50/-50°C)	Error of $\delta^{18}O_{fluid}$ (‰,VSMOW, +50/-50°C)
Cassiterite	Z6909_Cst_1.1	1.80E+09	0.001948548	5.15E-07	2.8	0.3	0.8	400	-3.8	6.6	-4.1/ -3.2	+0.3/ -0.6
Cassiterite	Z6909_Cst_1.2	1.78E+09	0.001948507	6.20E-07	2.8	0.3	0.8	400	-3.8	6.6	-4.1/ -3.2	+0.3/ -0.6
Cassiterite	Z6909_Cst_2.1	1.76E+09	0.001946936	6.13E-07	1.9	0.3	0.8	400	-3.8	5.7	-4.1/ -3.2	+0.3/ -0.6
Cassiterite	Z6909_Cst_2.3	1.73E+09	0.001946895	2.95E-07	1.9	0.1	0.7	400	-3.8	5.7	-4.1/ -3.2	+0.3/ -0.6
Cassiterite	Z6909_Cst_4.1	1.76E+09	0.001948206	4.07E-07	2.6	0.2	0.7	400	-3.8	6.4	-4.1/ -3.2	+0.3/ -0.6
Cassiterite	Z6909_Cst_5.1	1.77E+09	0.001948493	5.84E-07	2.8	0.3	0.8	400	-3.8	6.6	-4.1/ -3.2	+0.3/ -0.6
Cassiterite	Z6909_Cst_6.1	1.77E+09	0.001949602	5.46E-07	3.3	0.3	0.8	400	-3.8	7.1	-4.1/ -3.2	+0.3/ -0.6
Cassiterite	Z6909_Cst_7.1	1.75E+09	0.001945463	6.80E-07	1.2	0.3	0.8	400	-3.8	5.0	-4.1/ -3.2	+0.3/ -0.6
Cassiterite	Z6909_Cst_8.1	1.74E+09	0.00194717	6.95E-07	2.1	0.3	0.8	400	-3.8	5.9	-4.1/ -3.2	+0.3/ -0.6
Cassiterite	Z6909_Cst_9.1	1.75E+09	0.00194766	6.76E-07	2.3	0.3	0.8	400	-3.8	6.1	-4.1/ -3.2	+0.3/ -0.6
Cassiterite	Z6909_Cst_10.1	1.78E+09	0.001947822	4.93E-07	2.4	0.2	0.8	400	-3.8	6.2	-4.1/ -3.2	+0.3/ -0.6
Cassiterite	Z6909_Cst_10.2	1.76E+09	0.00194782	8.01E-07	2.4	0.4	0.8	400	-3.8	6.2	-4.1/ -3.2	+0.3/ -0.6
Cassiterite	Z6909_Cst_11.1	1.73E+09	0.001947265	4.25E-07	2.1	0.2	0.7	400	-3.8	5.9	-4.1/ -3.2	+0.3/ -0.6
Cassiterite	Z6909_Cst_13.1	1.74E+09	0.001945989	6.90E-07	1.5	0.3	0.8	400	-3.8	5.3	-4.1/ -3.2	+0.3/ -0.6
Cassiterite	Z6909_Cst_14.1	1.75E+09	0.001946585	8.96E-07	1.8	0.4	0.8	400	-3.8	5.6	-4.1/ -3.2	+0.3/ -0.6
Cassiterite	Z6909_Cst_14.2	1.75E+09	0.00194651	7.03E-07	1.7	0.4	0.8	400	-3.8	5.5	-4.1/ -3.2	+0.3/ -0.6
Cassiterite	Z6909_Cst_14.3	1.72E+09	0.001945331	8.35E-07	1.1	0.4	0.8	400	-3.8	4.9	-4.1/ -3.2	+0.3/ -0.6
Cassiterite	Z6909_Cst_15.1	1.73E+09	0.001947207	6.92E-07	2.1	0.3	0.8	400	-3.8	5.9	-4.1/ -3.2	+0.3/ -0.6
Cassiterite	Z6909_Cst_15.2	1.77E+09	0.001949539	1.06E-06	3.3	0.5	0.9	400	-3.8	7.1	-4.1/ -3.2	+0.3/ -0.6
Cassiterite	Z6909_Cst_16.1	1.78E+09	0.001949455	7.97E-07	3.2	0.4	0.8	400	-3.8	7.0	-4.1/ -3.2	+0.3/ -0.6
Cassiterite	Z6909_Cst_16.2	1.80E+09	0.001950168	5.19E-07	3.6	0.3	0.8	400	-3.8	7.4	-4.1/ -3.2	+0.3/ -0.6
Cassiterite	Z6909_Cst_16.3	1.79E+09	0.001949529	1.09E-06	3.3	0.5	0.9	400	-3.8	7.1	-4.1/ -3.2	+0.3/ -0.6
	average ± 2sd (n=22 out of 23)				2.4		1.4					
	Standard											
	YANKEE Cassiterite (average, n=8 out of 9)	1.72E+09	0.001947034	1.44E-06	2.0		0.7					

Table 5

Mineral	Stage	Mineral assamblege	Sample	^{16}O (CPS)	Raw $^{18}O/^{16}O$ Ratio	±2s	$\delta^{18}O$ (‰, VSMOW)	±2s (internal)	±2s (external)	Temperature (°C)	Fractionation factor (%)	$\delta^{18}O_{fluid}$ (‰, VSMOW)
Quartz	Intrusion	biotite granite	ZK2509-894	1.22E+09	0.001994865	2.33E-07	8.2	0.1	0.6	800	0.2	8.0
Quartz	Intrusion	biotite granite	ZK2509-894	1.23E+09	0.001994969	4.39E-07	8.2	0.2	0.6	800	0.2	8.0
Quartz	Intrusion	biotite granite	ZK2509-1065	1.22E+09	0.001995603	5.43E-07	8.5	0.3	0.6	800	0.2	8.3
Quartz	Intrusion	biotite granite	ZK2509-1296	1.19E+09	0.001995403	2.89E-07	8.4	0.1	0.6	800	0.2	8.2
Quartz	Intrusion	biotite granite	ZK2509-1296	1.22E+09	0.001995752	3.69E-07	8.6	0.2	0.6	800	0.2	8.4
Quartz	Early sulfide stage	Q+Fl+Ccp Vein	ZK2509-827	1.23E+09	0.001993635	4.96E-07	7.5	0.2	0.6	300	6.9	0.6
Quartz	Early sulfide stage	Q+Fl+Ccp Vein	ZK2509-827	1.24E+09	0.001995574	2.22E-07	8.5	0.1	0.6	300	6.9	1.6
Quartz	Early sulfide stage	Q+Fl+Ccp Vein	ZK2509-1065	1.23E+09	0.001995298	3.21E-07	8.4	0.2	0.6	300	6.9	1.5
Quartz	Early sulfide stage	Q+Mo vein	ZK0907-800	1.21E+09	0.00199323	3.72E-07	7.3	0.2	0.6	300	6.9	0.4
Quartz	Early sulfide stage	Q+Mo vein	ZK0907-800	1.24E+09	0.001992634	1.15E-07	7.0	0.1	0.6	300	6.9	0.1
Quartz	Early sulfide stage	Q+Mo vein	ZK0907-800	1.24E+09	0.00199345	3.64E-07	7.4	0.2	0.6	300	6.9	0.5
Quartz	Early sulfide stage	Q+Ccp+Asp	ZK2509-327	1.22E+09	0.002003452	3.34E-07	12.5	0.2	0.6	300	6.9	5.6
Quartz	Early sulfide stage	Q+Ccp+Asp	ZK2509-327	1.29E+09	0.001993584	3.42E-07	7.5	0.2	0.6	300	6.9	0.6
Quartz	Early sulfide stage	Qtz+Py+Mt+Amp	LG-46	1.21E+09	0.001985746	2.86E-07	3.5	0.1	0.6	300	6.9	-3.4
Quartz	Early sulfide stage	Qtz+Py+Mt+Amp	LG-46	1.21E+09	0.001981436	1.41E-07	1.4	0.1	0.6	300	6.9	-5.5
Quartz	Early sulfide stage	Qtz+Py+Mt+Amp	LG-46	1.22E+09	0.001986417	3.40E-07	3.9	0.2	0.6	300	6.9	-3.0
Quartz	Late sulfide stage	Q+Cal+Asp, Mt	HL21-06	1.25E+09	0.001978188	4.87E-07	-0.3	0.2	0.6	300	6.9	-7.2
Quartz	Late sulfide stage	Q+Cal+Asp, Mt	HL21-06	1.17E+09	0.001977661	5.05E-07	-0.5	0.3	0.6	300	6.9	-7.4
Quartz	Late sulfide stage	Q+Cal+Asp, Mt	HL21-06	1.23E+09	0.001976614	3.28E-07	-1.1	0.2	0.6	300	6.9	-8.0
Quartz	Late sulfide stage	Q+Cal+Asp, Mt	HL21-06	1.25E+09	0.00197682	4.92E-07	-1.0	0.2	0.6	300	6.9	-7.9
Quartz	Late sulfide stage	Q+Ccp+Sp+Cal+Fl	HL-38	1.21E+09	0.001972049	5.19E-07	-3.4	0.3	0.6	200	11.7	-15.1
Quartz	Late sulfide stage	Q+Ccp+Sp+Cal+Fl	HL-38	1.20E+09	0.001971114	4.59E-07	-3.9	0.2	0.6	200	11.7	-15.6
Quartz	Late sulfide stage	Q+Ccp+Sp+Cal+Fl	HL-38	1.23E+09	0.00197866	1.93E-07	0.0	0.1	0.6	200	11.7	-11.7

Quartz	Late sulfide stage	Q+Ccp+Sp+Cal+Fl	HL-38	1.22E+09	0.001971986	3.34E-07	-3.4	0.2	0.6	200	11.7	-15.1
Quartz	Late sulfide stage	Q+Sp+Cal	ZK1708-566 (core)	1.21E+09	0.001982501	1.66E-07	1.9	0.1	0.6	200	11.7	-9.8
Quartz	Late sulfide stage	Q+Sp+Cal	ZK1708-566 (rim)	1.24E+09	0.001980403	1.40E-07	0.8	0.1	0.6	200	11.7	-10.9
Quartz	Late sulfide stage	Q+Sp+Gn+Cal	HL-39-37	1.24E+09	0.001973059	2.70E-07	-2.9	0.1	0.6	200	11.7	-14.6
Quartz	Late sulfide stage	Q+Sp+Gn+Cal	HL-39-37	1.27E+09	0.001973114	2.81E-07	-2.8	0.1	0.6	200	11.7	-14.5
			Standard									
			NBS28 Quartz (average, n=13 out of 14)	1.25E+09	0.001997714	1.16E-06	9.6		0.6			
			UWQ1 Quartz (average, n=8)	1.23E+09	0.002003653	1.40E-06	12.6		0.7			
Calcite	Late Sulfide stage	Cal+Fl	HLWW-12	1.56E+09	0.001986075	4.93E-07	0.6	0.2	0.6	200	9.8	-9.2
Calcite	Late Sulfide stage	Cal+Fl	HLWW-12	1.56E+09	0.001985465	4.69E-07	0.3	0.2	0.6	200	9.8	-9.5
Calcite	Late sulfide stage	Q+Sp+Cal	ZK1708-566 (core)	1.63E+09	0.001980024	4.63E-07	-2.5	0.2	0.6	200	9.8	-12.3
Calcite	Late sulfide stage	Q+Sp+Cal	ZK1708-566 (rim)	1.60E+09	0.001979819	7.35E-07	-2.6	0.4	0.7	200	9.8	-12.4
			Standard									
			NBS19 Calcite (average, n=5)	1.53E+09	0.002041808	7.30E-07	28.6		0.4			

This is the peer-reviewed, final accepted version for American Mineralogist, published by the Mineralogical Society of America.
The published version is subject to change. Cite as Authors (Year) Title. American Mineralogist, in press.
DOI: https://doi.org/10.2138/am-2022-8523. http://www.minsocam.org/

Figure 1

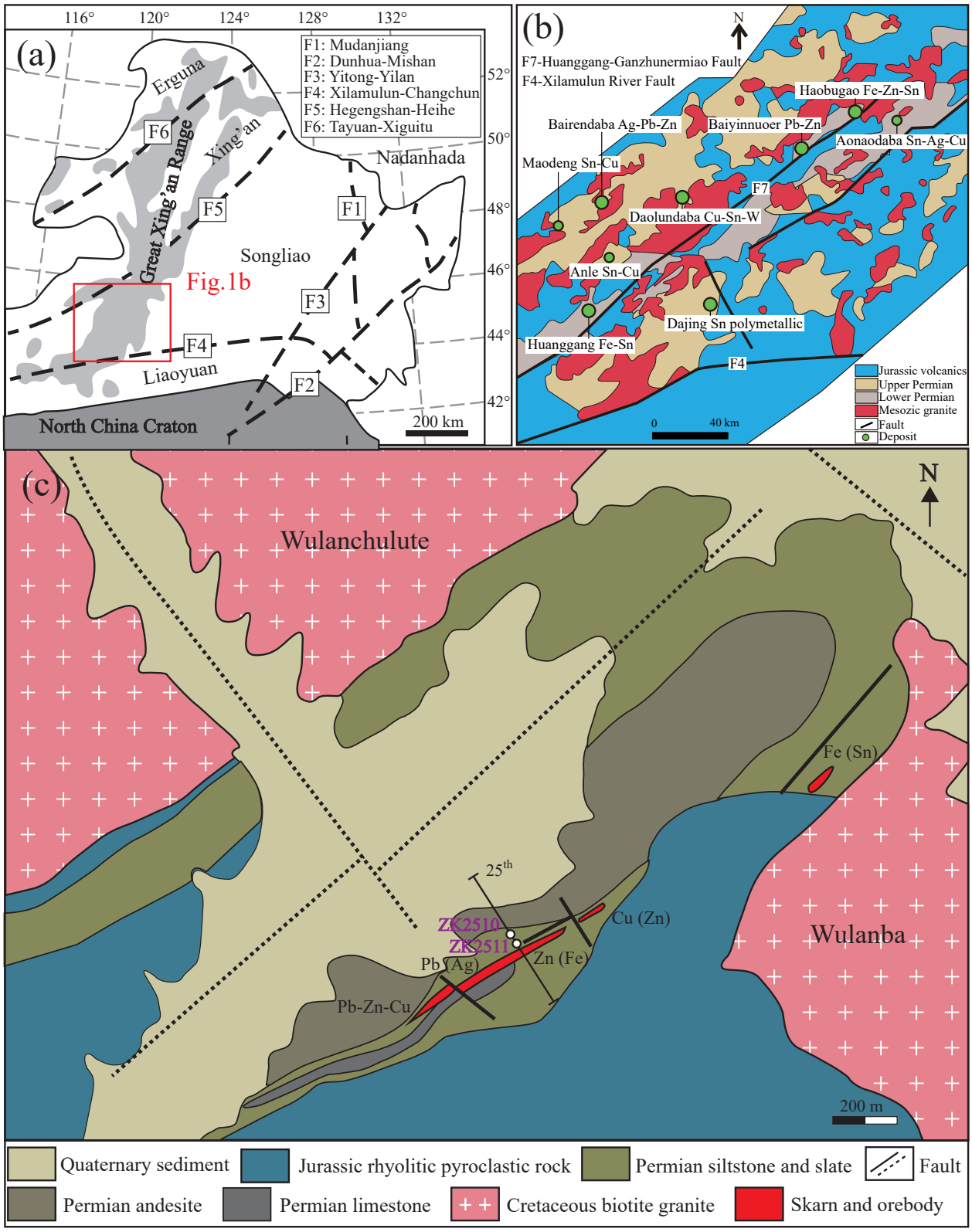

Figure 2

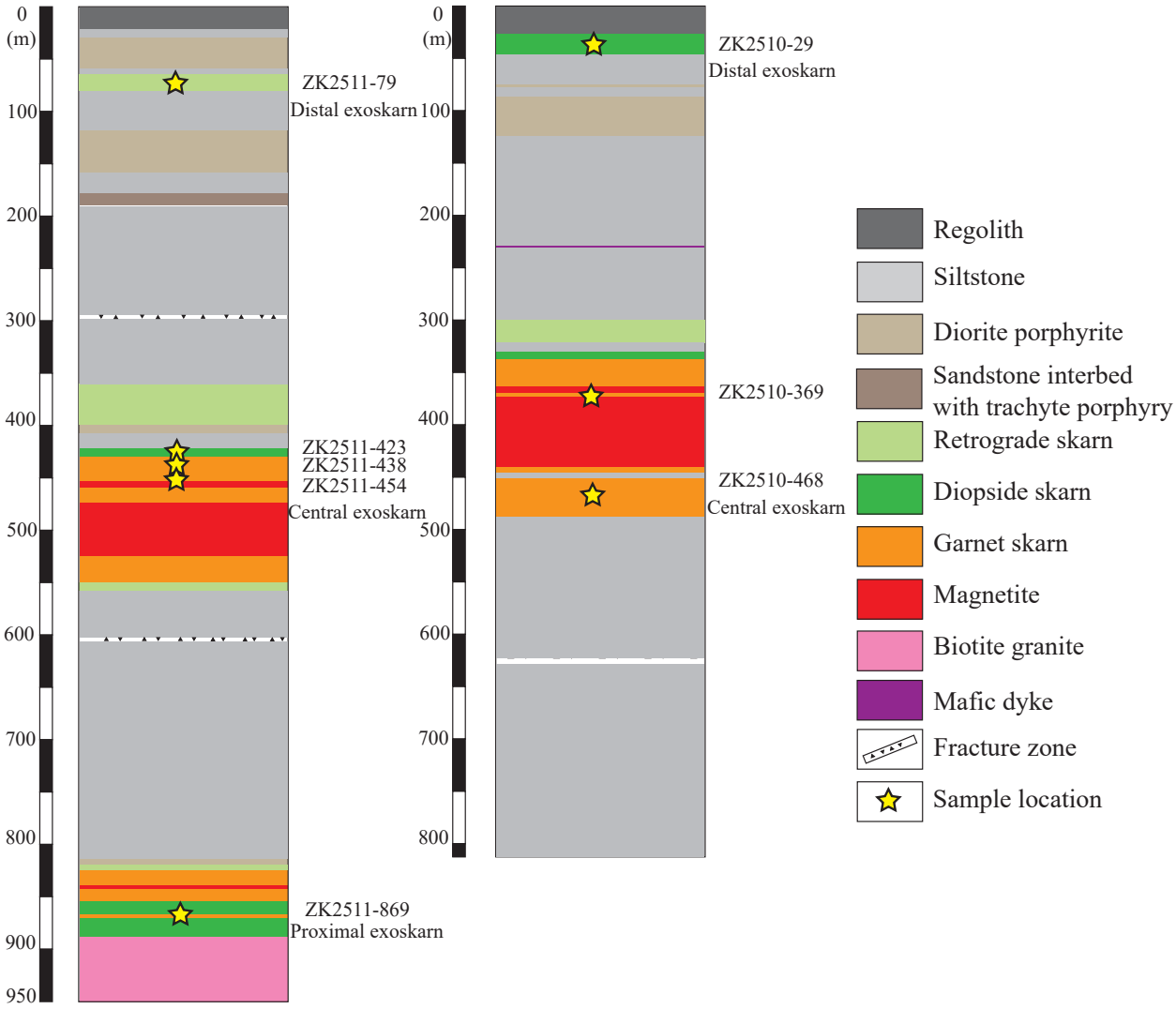

This is the peer-reviewed, final accepted version for American Mineralogist, published by the Mineralogical Society of America.
The published version is subject to change. Cite as Authors (Year) Title. American Mineralogist, in press.
DOI: https://doi.org/10.2138/am-2022-8523. http://www.minsocam.org/

Figure 3

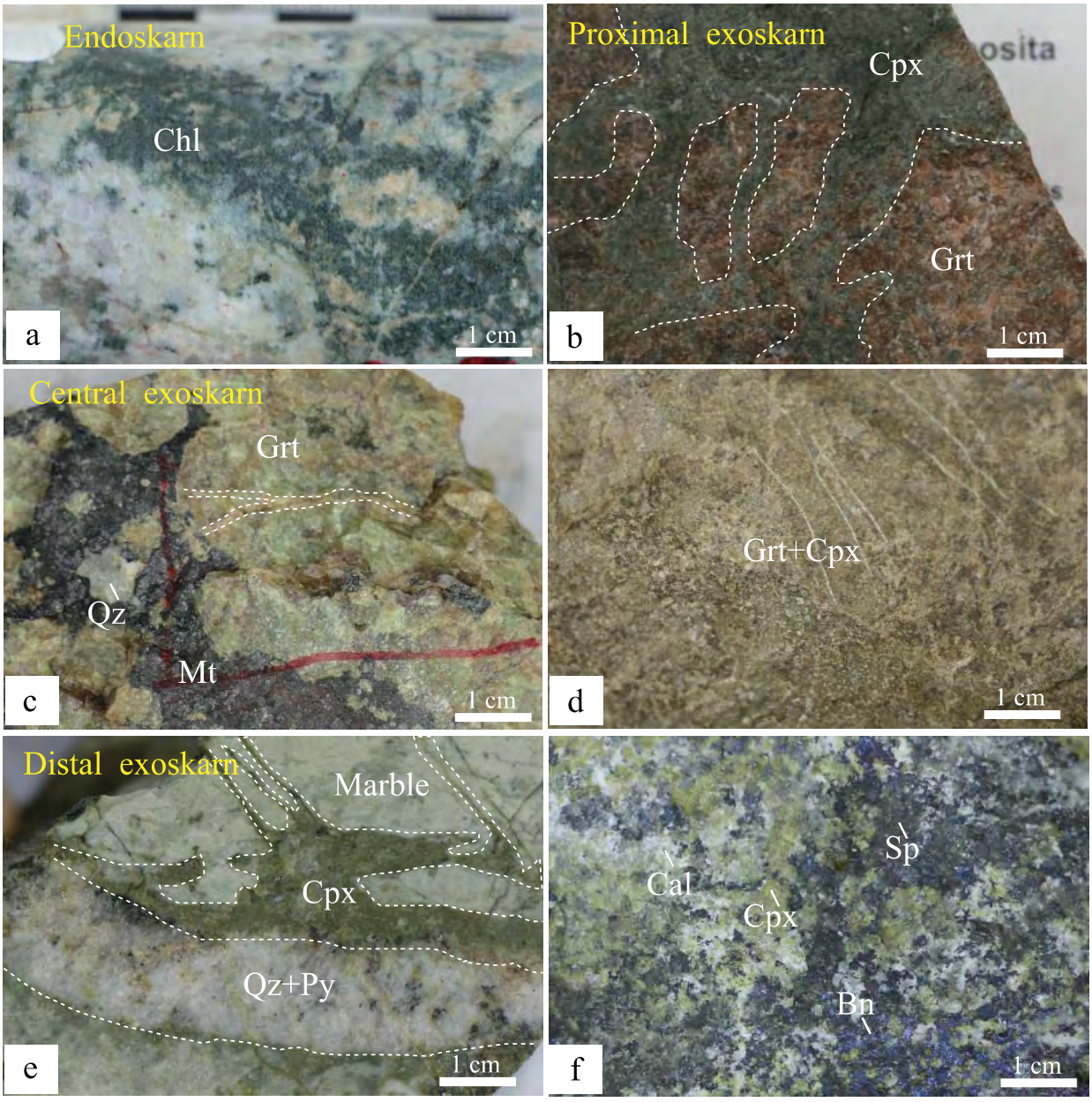

Figure 4

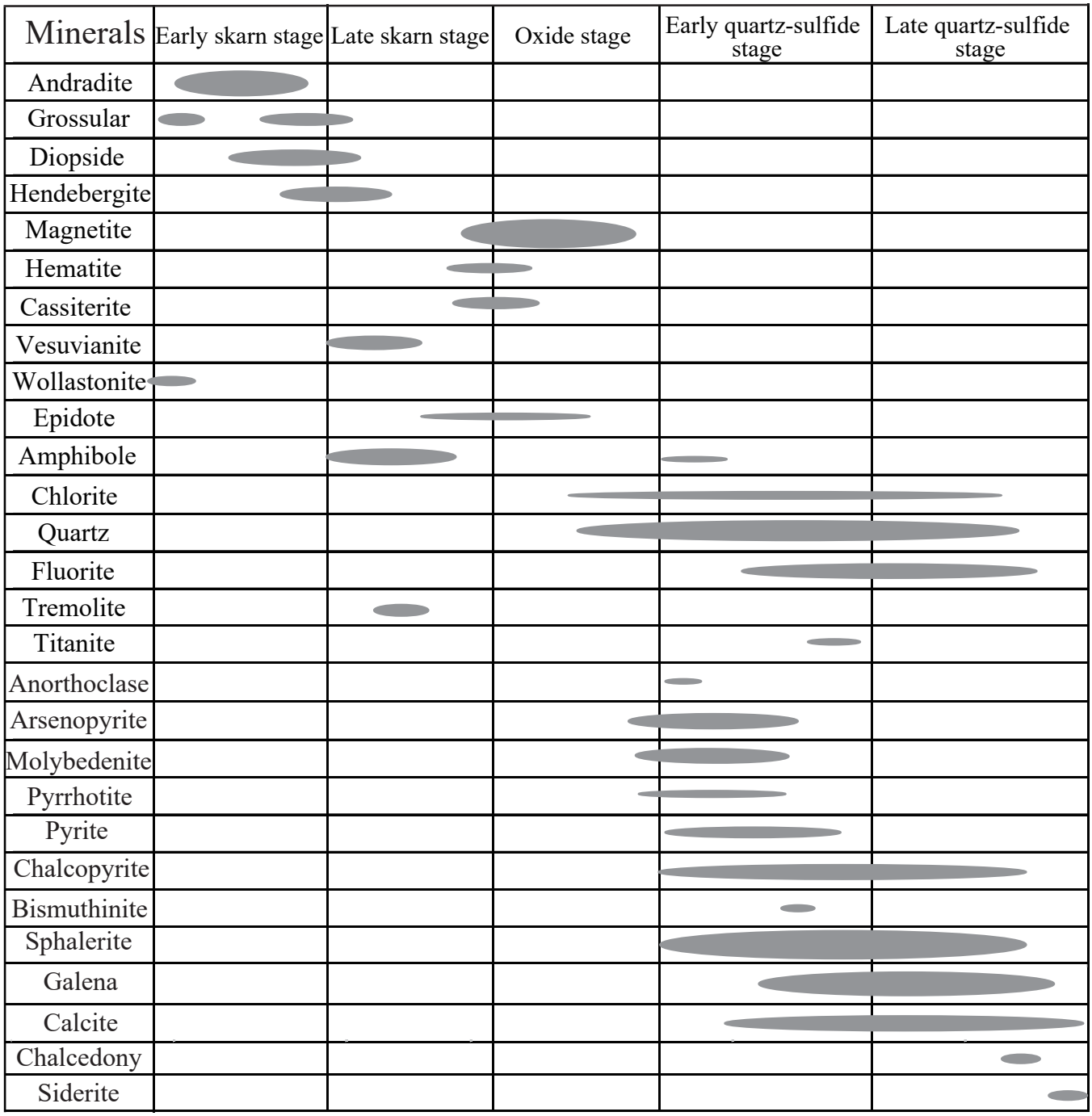

This is the peer-reviewed, final accepted version for American Mineralogist, published by the Mineralogical Society of America.
The published version is subject to change. Cite as Authors (Year) Title. American Mineralogist, in press.
DOI: https://doi.org/10.2138/am-2022-8523. http://www.minsocam.org/

Figure 5

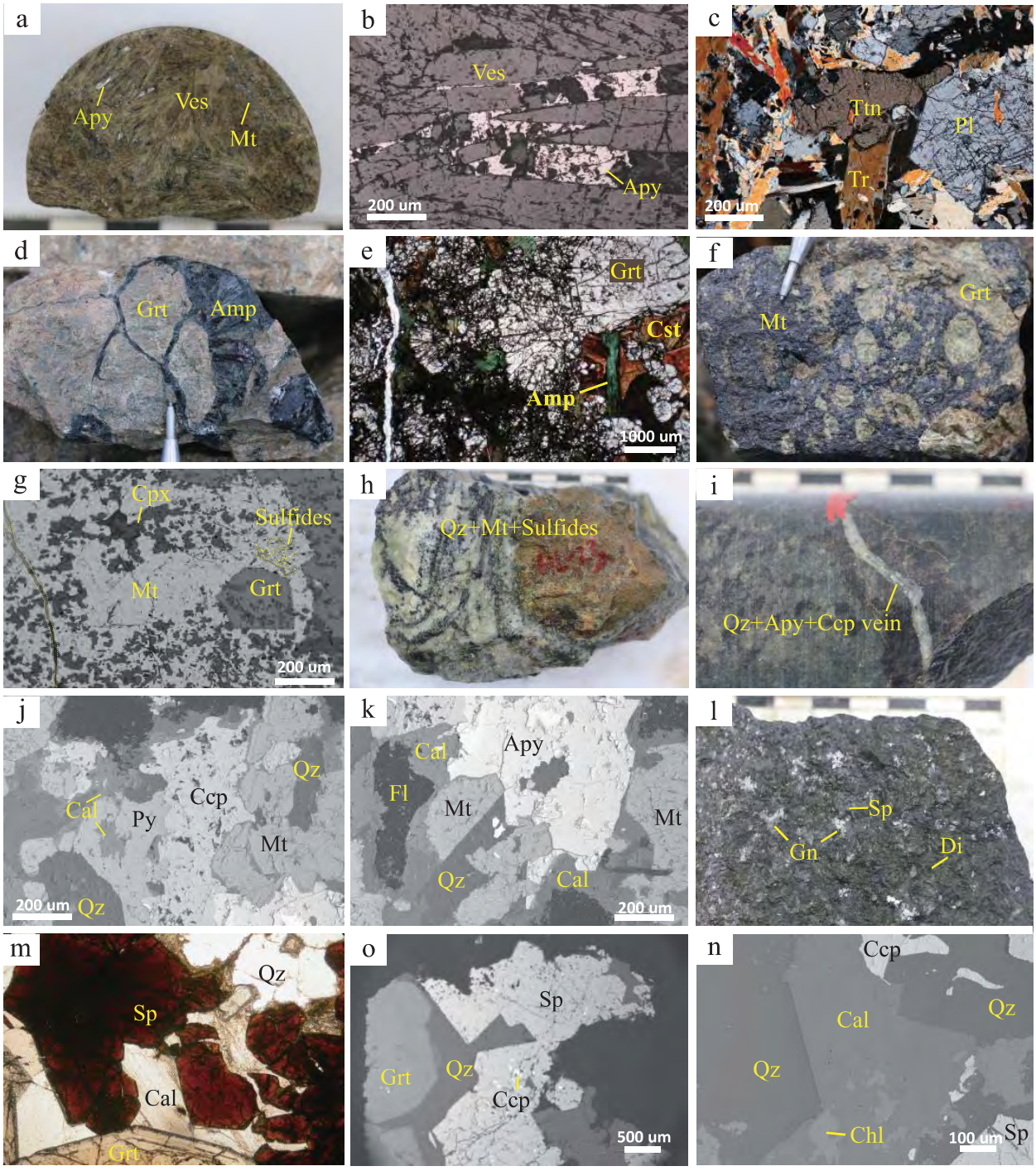

This is the peer-reviewed, final accepted version for American Mineralogist, published by the Mineralogical Society of America.
The published version is subject to change. Cite as Authors (Year) Title. American Mineralogist, in press.
DOI: https://doi.org/10.2138/am-2022-8523. http://www.minsocam.org/

Figure 6

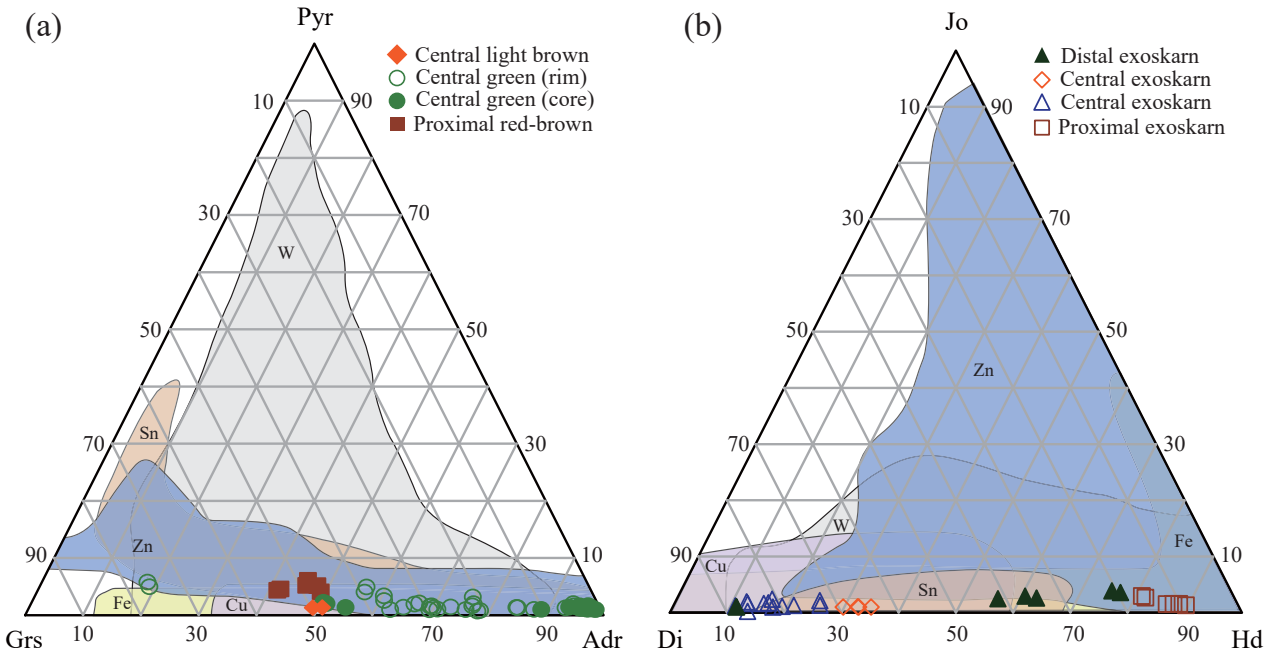

Figure 7

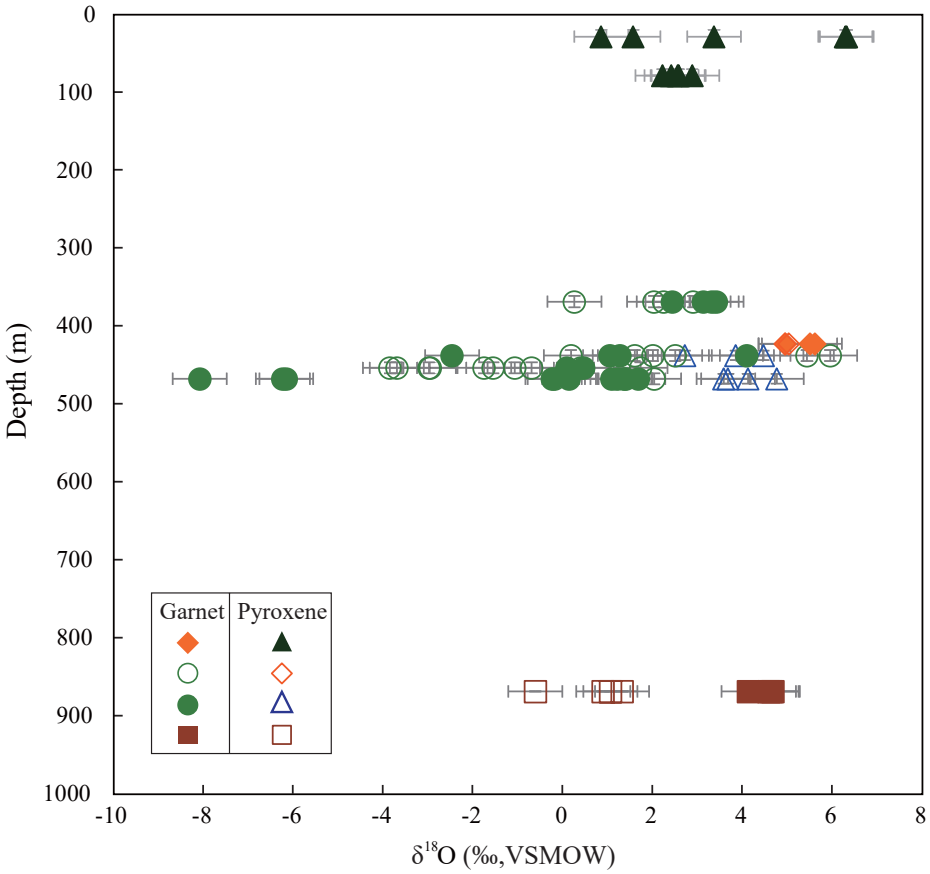

This is the peer-reviewed, final accepted version for American Mineralogist, published by the Mineralogical Society of America.
The published version is subject to change. Cite as Authors (Year) Title. American Mineralogist, in press.
DOI: https://doi.org/10.2138/am-2022-8523. http://www.minsocam.org/

Figure 8

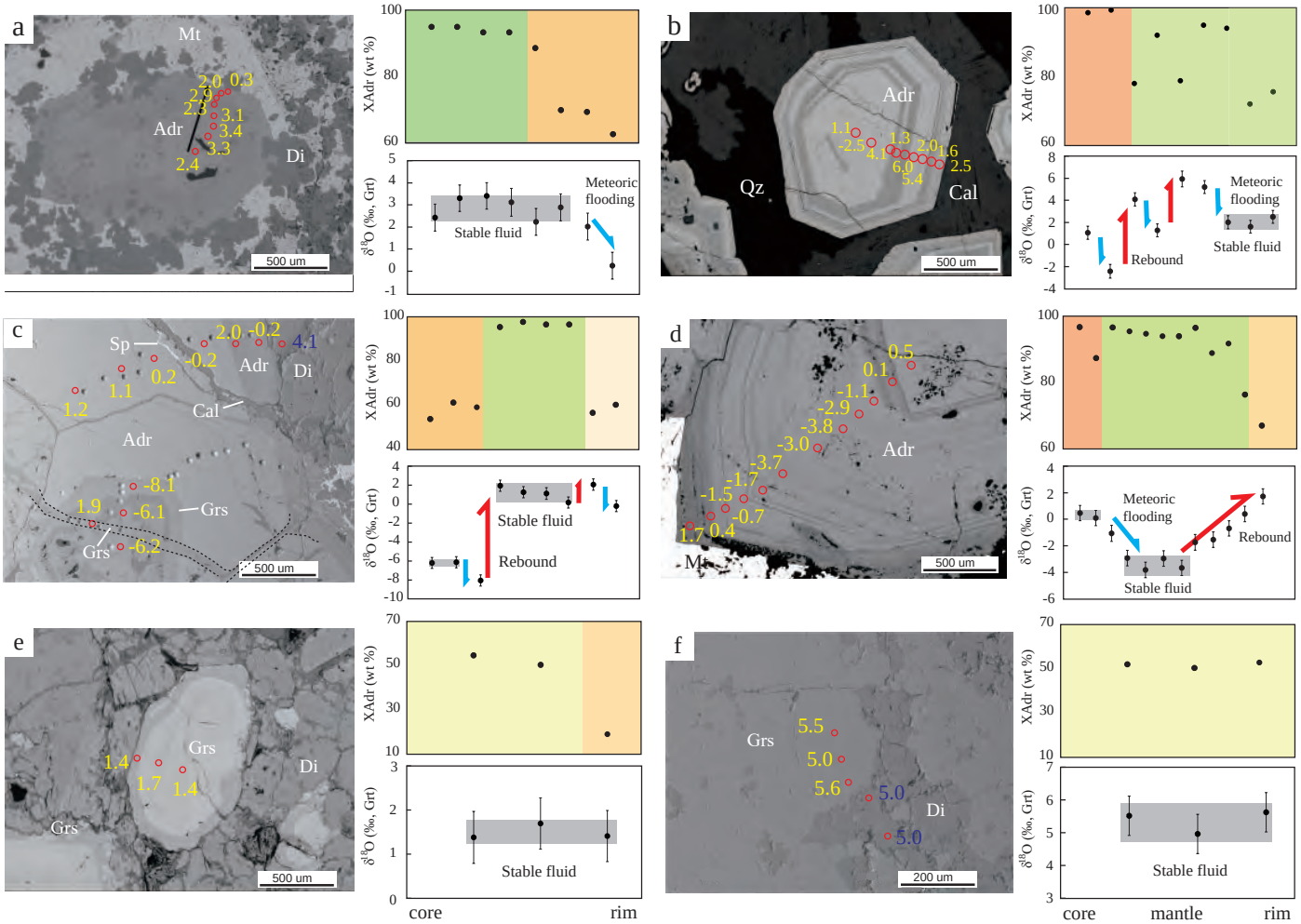

Figure 9

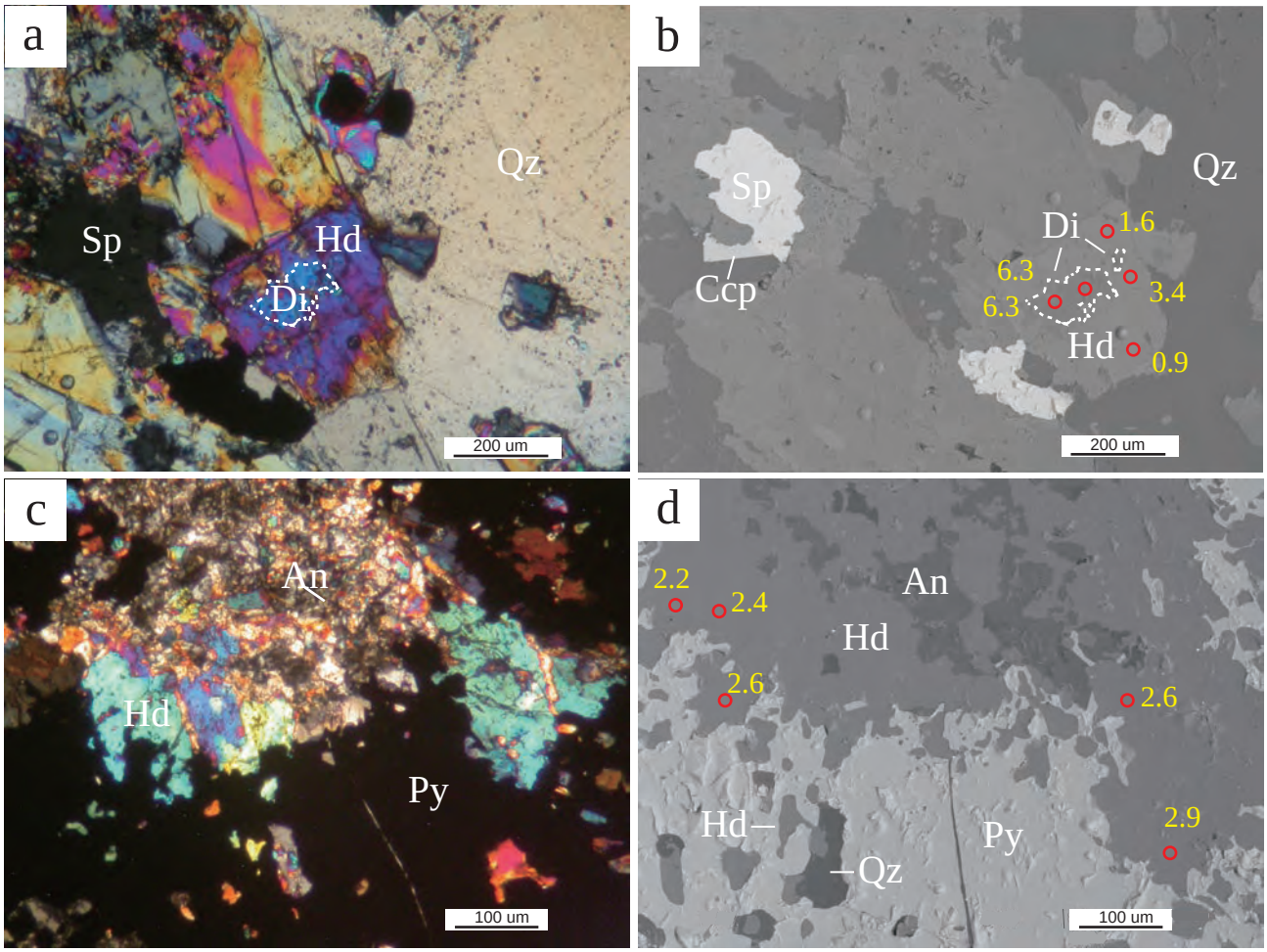

This is the peer-reviewed, final accepted version for American Mineralogist, published by the Mineralogical Society of America.
The published version is subject to change. Cite as Authors (Year) Title. American Mineralogist, in press.
DOI: https://doi.org/10.2138/am-2022-8523. http://www.minsocam.org/

Figure 10

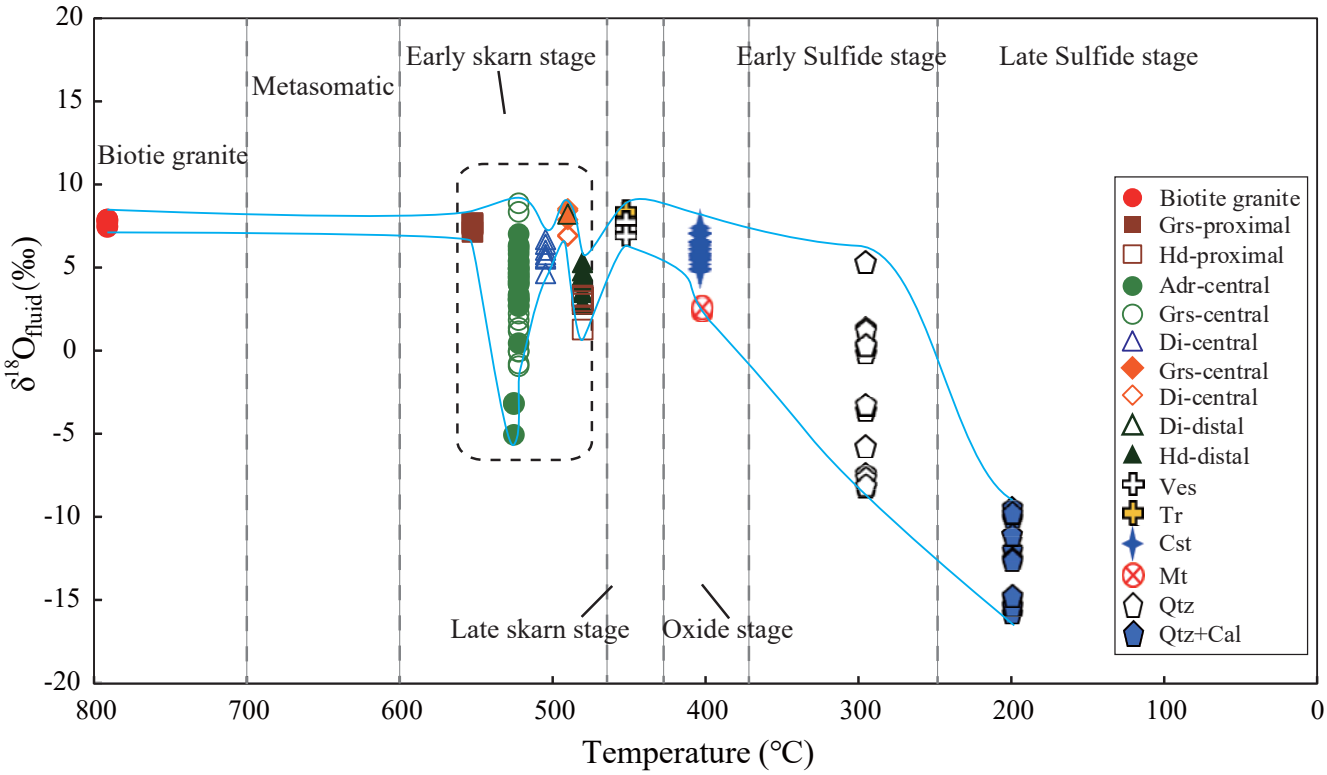

This is the peer-reviewed, final accepted version for American Mineralogist, published by the Mineralogical Society of America.
The published version is subject to change. Cite as Authors (Year) Title. American Mineralogist, in press.
DOI: https://doi.org/10.2138/am-2022-8523. http://www.minsocam.org/

Figure 11